Journal of Catalysis **196,** 18–39 (2000)
doi:10.1006/jcat.2000.3009, available online at http://www.idealibrary.com on IDEAL®

Understanding Homogeneous and Heterogeneous Contributions to the Platinum-Catalyzed Partial Oxidation of Ethane in a Short-Contact-Time Reactor

David K. Zerkle,* Mark D. Allendorf,† Markus Wolf,‡ and Olaf Deutschmann‡

*Los Alamos National Laboratory, Chemical Science and Technology Division, P.O. Box 1663, Mail Stop J567, Los Alamos, New Mexico 87545; †Sandia National Laboratories, Combustion Research Facility, Livermore, California 94551; and ‡Interdisziplinäres Zentrum für Wissenschaftliches Rechnen, Universität Heidelberg, Heidelberg, Germany

Received March 24, 2000; revised July 17, 2000; accepted August 2, 2000

This paper describes a computational study of the partial oxidation of ethane to ethylene in a short-contact-time reactor, using a two-dimensional computational fluid dynamics model with full heat and mass transport. Detailed heterogeneous and homogeneous chemical kinetic mechanisms are employed to describe the chemistry. Rate constants for elementary surface reactions are determined from literature sources or by fitting model predictions to experimental data. Simulations using these mechanisms suggest that platinum-catalyzed heterogeneous chemical processes are responsible for the oxidation of surface carbon and hydrogen, resulting in localized heat release into the gas phase. This heat release drives endothermic homogeneous and heterogeneous cracking of ethane to ethylene and H_2. The proportion of homogeneous and heterogeneous contributions depends strongly upon the reactor operating conditions. In addition to predictions of ethane conversion and ethylene selectivity, the model also predicts the production of all other major products: H_2O, H_2, CH_4, CO, and CO_2. A good fit is obtained between model predictions and experimental data for ethane/oxygen mixtures. The model is applied to ethane/hydrogen/oxygen mixtures and good agreement with this set of experimental data is also obtained.

Key Words: **ethane; partial oxidation; ethylene; oxidative dehydrogenation; catalysis; platinum; computational fluid dynamics; reactor simulation.**

INTRODUCTION

The recent application of so-called "short-contact-time reactors" (SCTR) to the autothermal production of ethylene from ethane (1) has lead to a promising new technology. In these devices, mixtures of ethane, O_2, and N_2 (with or without H_2) flow through a ceramic-foam monolith coated with a catalytic metal such as platinum. Mild heating of the reactor initiates an autocatalytic reaction that yields a mixture of ethylene, CO, H_2, and H_2O, with smaller amounts of CO_2, C_2H_2, CH_4, and higher hydrocarbons. The residence time in the reactor is typically less than 5 ms and reactor temperatures appear to be in the range 900–1000°C (1). Extensive experimentation (2–8) (see Discussion below) with the platinum-catalyzed system demonstrates that ethane conversion and ethylene selectivity comparable to conventional steam cracking can be achieved. Among the advantages of SCTRs are their small size and resistance to coking, which commonly plagues steam-cracking reactors.

Several experimental investigations suggest a dominant heterogeneous component to the mechanism. In the earliest experiments, performed by Huff and Schmidt (1), selectivities up to 70% and ethane conversions near 80% were observed for a $C_2H_6:O_2$ mole ratio of 1.7 with 20% N_2 dilution (Fig. 1; (1)). These authors speculated that the primary route to ethylene is through a surface ethyl group that undergoes β-hydrogen elimination. Experiments at pressures up to 5.5 atm (2) support this view and suggest that free-radical homogeneous-chain reactions are not significant within the range of pressures considered. Work by Yokoyama *et al.* (3) using tin alloyed to the platinum in the form of PtSn and Pt_3Sn showed that even higher ethane conversions and ethylene selectivities are possible, and the strong dependence on catalyst composition was considered evidence of a dominant heterogeneous mechanism for the ethane oxidative dehydrogenation process. Finally, Witt and Schmidt (4) found that flow rate has little influence on ethane conversion, ethylene selectivity, and CO selectivity, arguing against direct decomposition from ethane to CO via ethylene, suggesting instead that parallel reaction pathways to ethylene and CO are involved.

An interesting set of experiments was performed by Flick and Huff (5) at $C_2H_6:O_2$ mole ratios as low as 1.2, which are lower than those normally used to obtain optimum ethylene yield (typically 1.5–1.7). These experiments showed that acetylene is produced in relatively high concentrations, with more acetylene observed as the reactant mixture becomes more fuel-lean. The authors argued that a homogeneous mechanism is responsible for the increased acetylene selectivity because the reaction temperature under these fuel-lean conditions is higher. They also speculated that

0021-9517/00 $35.00

adsorbed hydroxyl radicals desorb under these conditions, leading to homogeneous free-radical chain reactions that result in acetylene formation.

The effects of adding a washcoat and changing the ceramic support material, pore size, and platinum loading were investigated experimentally by Bodke *et al.* (6). Adding a thin γ-alumina washcoat was shown to have the greatest impact, reducing the ethylene yield significantly while increasing the selectivity to CO, while changing the catalyst loading had little effect. The washcoat adds microporosity to the monolith surface and increases the surface area by a factor of 10 (6). Because ethylene is a nonequilibrium product of the original ethane and oxygen mixture, it was argued that the ethylene produced must exit the reactor as fast as possible to achieve high selectivity. The effect of the washcoat is to trap ethylene produced at the surface, allowing it to react further to form CO. The authors again concluded that homogeneous chemistry plays a minor role in the partial oxidation of ethane to ethylene.

In contrast to these earlier investigations, experiments conducted by Bodke *et al.* (7) on the platinum–tin alloy system suggest that both homogeneous and heterogeneous chemistries play a role in the conversion of ethane to ethylene. The authors report the addition of H_2 to the reactant feed mixture for the first time; they obtained an ethylene selectivity of 85% with ethane conversion greater than 70% using a $C_2H_6 : H_2 : O_2 = 2 : 2 : 1$ mixture. The authors concluded that the improved performance is the result of preferential oxidation of H_2 to H_2O at the expense of ethane oxidation. The most promising mechanistic scenario is heterogeneous hydrogen oxidation followed by oxygen-free homogeneous ethane dehydrogenation, although the reported time scale ($\sim$10 ms) required for this process is longer than that thought to be characteristic of the SCTR ($<$5 ms) (7). In a later publication, Bodke *et al.* (8) extended the experiments to include various physical forms, including alumina spheres and fibermats. The authors also report the selectivity to C_3H_6, C_3H_8, C_4H_8, and C_4H_{10} over Pt and find that the summed selectivity to these species is approximately 5% under all of the conditions studied.

Many additional ethane dehydrogenation experiments have been performed with a variety of configurations and results for both Pt systems (9–11) and non-Pt systems (12–15). The comparison between Pt-coated monoliths and pellets for the oxidative dehydrogenation of ethane at short contact time was made by Flick and Huff (9), who report nearly identical performance ($\sim$70% ethane conversion, $\sim$60% ethylene selectivity) for these physical forms at low (20%) N_2 dilution. These authors also report the temperature measured near the front of the reactor to be higher than that measured near the exit. Lødeng *et al.* (10) studied ethane and propane oxidative dehydrogenation at 10^{-5}-s contact times in Pt and Pt/Rh gauze reactors and report ethane conversion of $\sim$50% with ethylene selectivity of $\sim$65% over the Pt gauze. These authors argue that gas-phase reactions are dominating the chemistry under these conditions, with the gauze catalyzing oxidation that provides heat for gas-phase dehydrogenation. A comparison between supported chromium oxide and Pt-coated monoliths was made by Flick and Huff (11), and they report excellent ethane oxidative dehydrogenation performance for the chromium oxide system ($\sim$80% ethane conversion, $\sim$70% ethylene selectivity), rivaling that of the Pt–Sn system of Bodke *et al.* (7). Flick and Huff speculate that the front part of the monolith is in an oxidizing environment where heat is released so that endothermic dehydrogenation takes place in the reducing environment near the end of the monolith. These authors give support for heterogeneous reactions dominating the chemistry, but do not rule out gas-phase reactions, especially under the higher temperature conditions.

Morales and Lunsford (12) studied the oxidative dehydrogenation of ethane over a lithium-promoted magnesium oxide catalyst in a fixed-bed reactor at long residence time (GHSV = 260 1/h). They report ethane conversion of 40% and ethylene selectivity of 75% at 600°C and conclude that homogeneous reactions become dominant at 675°C with ethyl radicals generated by the surface emanating into the gas phase where they react with O_2 to form ethylene. In a similar Li/MgO experiment with results published in the same year, Martin *et al.* (13) report on the conversion of methane and C_2 hydrocarbons. Ethane conversion of $\sim$50% and ethylene selectivity of $\sim$70% are reported, with significant participation in the gas phase. However, these authors argue against the notion that methyl and ethyl radicals generated by the surface are important for the gas-phase chemistry. In a later study of ethane conversion over Li/MgO and Sn/MgO catalysts at long residence times, Burch and Crabb (14) report that the noncatalyzed oxidative dehydrogenation of ethane is at least as good as that on any known pure (nonpromoted) oxide catalyst, in contrast to the results of Morales and Lunsford (12). These authors report ethane conversion of 45% with an ethylene selectivity of 73.7% at 600°C and argue that the process is entirely in the gas phase under these conditions.

Baerns and Buyevskaya (15) present a thorough summary of the most viable ethane oxidative dehydrogenation techniques and report specific research results for rare-earth oxide-based (REO) catalysts. Ethane conversion of 67% with ethylene selectivity of 68.3% is reported for a Na–P/Sm_2O_3 ($P : Na : Sm = 1 : 2 : 70$) catalyst in a nonisothermal reactor with a temperature maximum of 867°C and contact times of $\sim$30–40 ms. These authors conclude that oxidation reactions on REO catalysts provide sufficient heat for thermal pyrolysis of ethane that most probably occurs in the gas phase.

The role of homogeneous reactions in the oxidative dehydrogenation of propane over Pt at short contact time has

also been studied (16–18). In reports focused on the influence of mass transfer limitations in a variety of reactor configurations (16) and homogeneous reactions in annular reactors (17), Beretta *et al.* find that only complete oxidation products of propane are measured at temperatures lower than 500–600°C. Above 500–600°C, these authors report a dramatic rise in propane conversion, accompanied by increases in propylene and ethylene selectivities and decreases in the CO_2 and H_2O selectivities. Beretta *et al.* conclude that if the reactor temperature is high enough, then gas-phase reactions alone can explain the production of olefins from propane, while the Pt-catalyzed oxidation provides heat. This conclusion is supported by subsequent work (18) in which an annular reactor is designed for autothermal propane oxidative dehydrogenation. Beretta *et al.* (18) also report the results of an adiabatic plug flow simulation, i.e., infinitely fast radial transport of heat and mass with no axial diffusion of heat or mass, with a specified preheat of $T_{in} = 327$°C and purely homogeneous chemistry. The results of these simulations agree well with the experimental results for the autothermal reactor, except that the required residence time was approximately twice as long in the simulation as was observed in the experiment. While these results support the notion of gas-phase olefin production, the authors (18) acknowledge that catalytic production of olefins is possible and could be responsible for the shorter experimental residence time.

In addition to the experiments just described, there have been a number of efforts to develop computational models of the SCTR. Hickman and Schmidt (19) performed the earliest simulation of an SCTR system for conversion of methane to synthesis gas. This model assumes tubular plug flow. In addition, it was assumed that temperature was uniform throughout the reactor and that it could be determined from a heat balance consistent with the reactor exit-product distribution. Using a purely heterogeneous mechanism, these authors were able to predict CO and H_2 product selectivities that are consistent with the selectivities observed experimentally. Huff and Schmidt (20) extended the model of Hickman and Schmidt to simulate ethane conversion to ethylene, again using only heterogeneous chemistry. The results of these simulations are in reasonable agreement with the experimental data (1), but it was necessary to add an explicit steam-reforming reaction of surface carbon, suggesting that this process is important in this reaction system. Despite the absence of homogeneous chemistry in this model, the authors recognized that the actual mechanism might be a combination of heterogeneous and homogeneous processes.

Wolf *et al.* (21) studied mass and heat transfer limitations to the partial oxidation of methane over a Pt/MgO catalyst, comparing experimental results to simulations employing a simple four-step heterogeneous kinetic model and one-dimensional plug flow analysis. These authors report that modeling the axial conduction of heat in the reactor wall broadens the wall temperature profile and reduces the peak wall temperature from 1700 to 1380 K. No significant contribution from radiation heat transfer is reported, even at temperatures as high as 1380 K. Veser and Frauhammer (22) modeled ignition and steady-state catalytic methane oxidation over Pt in a monolith reactor. A multistep heterogeneous kinetic mechanism is proposed, and agreement between one-dimensional plug flow simulations and experimental results is demonstrated. The authors report that gas-phase reactions do not play a major role in methane conversion in this catalytic system.

Deutschmann and Schmidt (23) achieved a significant advance in SCTR simulations for the partial oxidation of CH_4 to synthesis gas on rhodium. These authors were able to model the reactor in two dimensions with full mass transport and heterogeneous reaction chemistry using FLUENT (24) coupled with external FORTRAN subroutines to simulate coverage-dependent surface reactions. In the gas phase, full heat transport was employed, but an isothermal condition was imposed on the wall with the temperature chosen to be consistent with experimental observations. The simulations show that a complex interaction exists between heterogeneous chemistry and the reactor mass and heat transfer, especially at the catalyst entrance, where extremely rapid variations in temperature, velocity, and transport coefficients are observed. Deutschmann and Schmidt (25) were later able to include homogeneous chemistry in their two-dimensional simulations of CH_4 partial oxidation on both rhodium and platinum. The results indicate that homogeneous reactions strongly affect CH_4 conversion and synthesis-gas selectivities only when the reactor pressure in the simulation was raised to 10 bar. It is worth noting that these authors observed a dramatic increase in the total computational time required to achieve converged solutions when detailed homogeneous chemistry was employed.

Recently, Huff *et al.* (26) published a quantitative assessment of the role of homogeneous chemistry in Pt-catalyzed ethane conversion at short contact time. A multistep heterogeneous mechanism is employed along with a homogeneous mechanism in a plug flow analysis to simulate the results of ethane oxidative dehydrogenation experiments. The agreement between simulation results and the experiments is good. The authors' results indicate that all of the ethylene produced in the simulations originates from endothermic gas-phase reactions, the heat for which is provided by catalytic ethane oxidation. This is in general agreement with the results of Beretta *et al.* (16–18) for propane conversion. However, because the heterogeneous kinetic mechanism employed by Huff *et al.* (26) does not include an ethylene desorption step, it is inevitable that the simulations show all of the ethylene being produced homogeneously under all conditions. In addition, these authors recognize

that heat transport strongly influences the reactor temperature profile (which in turn can strongly influence the rate of gas-phase reactions). Unfortunately, heat conduction in the reactor wall is not modeled accurately in the reported plug flow analysis (26) and, as demonstrated by Wolf *et al.* (21), this simplification can have a dramatic effect on the calculated peak wall temperature.

This paper describes results of SCTR simulations of C_2H_6/O_2 mixtures that for the first time include both heterogeneous and homogeneous chemical–kinetic processes coupled to a two-dimensional flow-field model with full heat and mass transport. The effects of H_2 addition to the feed are also discussed. Rate constants for the elementary reactions in the heterogeneous mechanism are obtained through a combination of literature values, theoretical estimates, and fits to experimental data. The results indicate that both gas-phase and surface chemical reactions play key roles in the conversion of ethane to ethylene, while heterogeneous processes dominate the subsequent formation of undesired products, such as CO, CO_2, and CH_4. These simulations also support the mechanism proposed by Bodke *et al.* (7) describing the effects of H_2 addition, but indicate that interactions between mass transport and chemistry determine the time scale for the process. Importantly, the results of this investigation suggest that the comprehensive modeling approach described here is essential to accurately simulate the production of ethylene in a SCTR.

COMPUTATIONAL METHODS

Reactor Flow Modeling

We simulate the performance of ethane SCTRs with a fluid-flow model coupled to heterogeneous and homogeneous chemical kinetics, using full heat and mass transport in a two-dimensional, axisymmetric flow field. The fluid and heat transport are modeled using FLUENT (24), with a methodology similar to that used previously (23, 25). To simulate the SCTR, FLUENT solves the two-dimensional steady-state Navier–Stokes equations cast in a cylindrical coordinate system. The time required to obtain converged solutions, with both heterogeneous and homogeneous chemistries included, varies from 30 min to 6 h using standard workstations (Silicon Graphics Indigo II with an R10000 CPU running at 175 Mhz or a Dell personal computer with an Intel Pentium II CPU running at 400 Mhz). For comparison, the solution of the nonreacting flow for this geometry with a heated wall requires less than 30 s to converge. The solution time increases by only a factor of 2 when homogeneous chemistry is included in the model, in contrast with the factor of 30 or more reported previously (25). A possible explanation for this will be discussed in a later section.

The experimental reactor geometry along with the representation of a monolith pore used in the calculations is shown schematically in Fig. 1. The axisymmetric-channel model serves as a reasonable geometric simplification for the tortuous path of a single, continuously connected pore within the ceramic-foam monolith. The results to be presented in this paper indicate that the majority of both the surface- and gas-phase reactions have reached completion within the first 1–2 mm of the channel. The tortuousity over this dimension is mild. Experiments involving alternative support geometries (8, 9) indicate that the physical form of the support does not play a significant role in the reactor performance under the conditions studied here and that straight channel monoliths, although more difficult to work

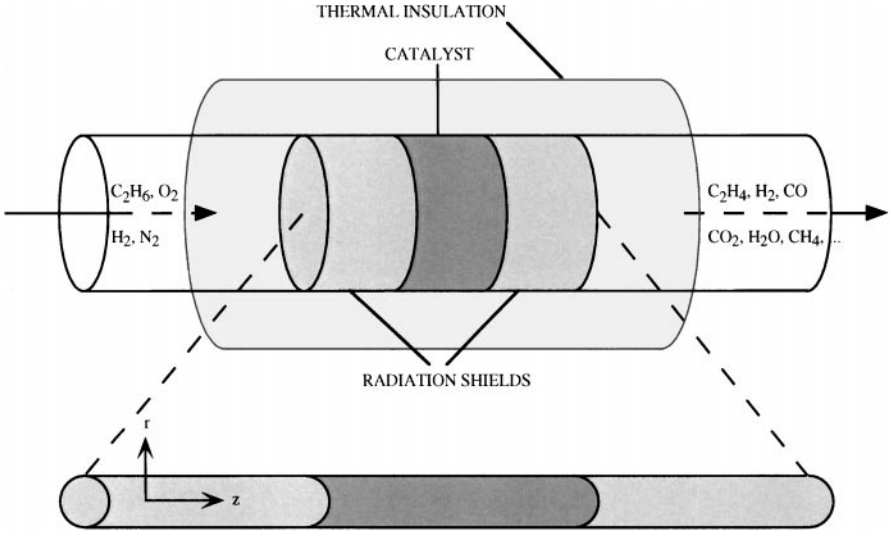

FIG. 1. Schematics of the experimental SCTR, showing the heat shields and central catalytic section (top) and the single-pore reactor model (bottom).

with, perform similarly to foam monoliths (27). Conditions under which the straight channel simplification might fail include high N_2 dilution for a pelletized reactor bed (9) and extremely high space velocity ($\sim$100 times that considered here) such that the reacting zone is moved toward the reactor exit.

The catalytic section of the reactor is 1 cm long and there are 1-cm-long, noncatalytic alumina sections that serve as heat shields upstream and downstream of the catalytic section. The catalytic section is modeled as an α-alumina ceramic substrate having a monolayer coverage of platinum, resulting in a surface-site density of $\rho_s = 1.64 \times 10^{19}$ sites/m^2 (from the density of bulk platinum). The heat shields do not have a platinum coating, but are geometrically identical to the catalytic section. In the experiments simulated here (6, 8), the monoliths contained 45 pores per linear inch (ppi), which corresponds to a single-pore channel diameter of 0.5 mm and a wall thickness of 0.0625 mm. The axisymmetric geometry is spatially discretized on a structured grid with 83 cells in the axial direction and 18 cells in the radial direction. The grid is nonuniform, having a greater density of computational cells near the wall and near the entrance to the catalytic section. In these regions we find the largest gradients for the dependent variables and thus the greatest spatial resolution is required here.

Of particular importance is the method used for including heat transport in the reactor wall and calculating the wall temperature profile. Heat generated by surface chemical reactions is deposited into the gas-phase computational cell nearest the wall. Flow velocity here is quite small, and heat is readily transferred to the first computational cell within the wall. Within the wall heat can conduct both upstream and downstream. Thus the temperature at any given point along the wall is influenced by the temperature at all other points, as well as the net gas-surface heat transfer rate at all points. Radial conduction of heat in the wall is also modeled, but the radial temperature gradient is small in near adiabatic conditions. We impose a small external heat loss so that the reactor exit temperature is $\sim$50 K below the adiabatic temperature, which is consistent with experimental observations (6). The thermal conductivity of the wall material is 33 W/m^{2}K, which is an average value based on the 92% alumina, 8% silica makeup of this ceramic.

The total flow rate of reactants in the experiments was typically 5 slpm (6), which results in a single-pore axial velocity of approximately 32 cm/s for mixtures of ethane and O_2 at the inlet conditions (298 K, 1.2 atm). Laminar flow (Re $\sim$20) results from the low flow speed and small diameter of the channel. With the exception of the specific heat, laminar fluid properties are calculated as functions of temperature and composition and are based on ideal-gas kinetic theory. Kinetic-theory size parameters and potential-energy factors for all gas-phase species are taken from the CHEMKIN transport database (28). For specific heats we use the CHEMKIN thermodynamics database (29) to calculate specific heat as a function of temperature and then describe this variation in a piecewise-linear fashion within FLUENT.

Heterogeneous Chemistry Model

The model for heterogeneous chemistry built into FLUENT is not capable of calculating fractional coverages of surface species (24). This capability is necessary to incorporate the detailed heterogeneous mechanism presented in a later section. For this reason we couple the main executable FLUENT code to external FORTRAN subroutines that model heterogeneous chemistry (25). Chemical reactions occurring on the surface both consume and produce gas-phase species. In addition, heat is released or consumed as a result of these reactions. The net result of the external subroutines is to construct source terms consistent with the reactions occurring on the surface. These source terms are included in the FLUENT conservation equations for each gas-phase species and for enthalpy. The solution for surface coverages is obtained in the same way and with the same external subroutines as in Deutschmann and Schmidt (25).

Homogeneous Chemistry Model

For the gas-phase chemistry we use a methodology very similar to that described above for surface chemistry. A detailed kinetic mechanism is employed consisting of modified Arrhenius expressions, which can be subject to third-body collision enhancement factors, low-pressure treatments, and a Troe (30) bimolecular pressure fall-off treatment. The gas-phase-chemistry capability within FLUENT is more advanced than that for surface chemistry; however, it still lacks the flexibility to allow for pressure-dependent reactions. Therefore, we again rely on external subroutines to interpret the gas-phase kinetic mechanism and develop species and enthalpy source terms needed by FLUENT.

In a departure from the procedure for handling surface chemistry in the external subroutines, we do not rely on a pseudo-time integration in order to estimate net rates for each species and to provide numerical stability (25). Instead, we employ a direct calculation of chemical source terms and then impose an underrelaxation factor on the change in the source-term values from one global FLUENT iteration to the next. We find that this procedure results in very stable numerical convergence behavior. It also permits the inclusion of homogeneous chemical reactions without drastically increasing the computational time required for convergence to the steady state.

CHEMICAL MECHANISMS

Homogeneous Chemical Mechanism

The detailed mechanism describing the gas-phase chemistry that we use is a subset of a much larger reaction set developed by Marinov *et al.* (31) for prediction of combustion behavior in rich CH_4 and ethane flames. The complete mechanism consists of 161 species involved in 722 reactions. In the interest of minimizing computation times, we reduced this to a subset containing the bulk of the C_1 and C_2 chemistry in Marinov's mechanism, which comprises 25 reactive species involved in 131 reversible reactions and 1 irreversible reaction. Not included in this subset are the reactions involving CH, CH_2 (singlet), CH_2OH, C_2, C_2H, C_2O, and HCCOH. Although some of these species can be important in rich hydrocarbon flames, particularly those in which acetylene is a fuel or there is soot formation (32), we find that their omission does not significantly alter the concentrations predicted by the full mechanism for typical SCTR operating conditions. In particular, this subset satisfactorily reproduces the predictions of the full mechanism in transient isothermal ethane pyrolysis calculations using SENKIN (33), with typical deviations in major species concentrations of no more than 25% and maximum deviations of approximately a factor of 2 for some minor species. The reduced mechanism also accurately predicts measured flame speeds (34) in rich CH_4 and ethane flames at pressures up to 3 atm using PREMIX (35). Finally, the model predicts trends in reactant and product concentrations as a function of temperature (950–1250 K) that are in reasonable agreement with those measured by Dagaut *et al.* (36) in a jet-stirred reactor for the oxidation of ethane. Details of this modeling will be discussed in a separate paper (37).

Heterogeneous Chemical Mechanism

A detailed heterogeneous kinetic mechanism, consisting of 19 surface species and 82 elementary reactions, was developed to simulate the reaction of $C_2H_6/H_2/O_2$ mixtures in SCTRs (Table 1). The kinetic data for the reactions in this mechanism were obtained by combining previously reported kinetic data on platinum for hydrogen oxidation on platinum (38–41) and oxygen-free conversion of methane to ethane (42). To these a third reaction set was added that describes the oxidation of carbon-containing species.

Extensive study has previously gone into understanding the mechanism by which ethane hydrogenolysis, ethylene hydrogenation, and hydrocarbon decomposition occur on platinum (43–54). Estimates and measurements of reaction energetics are included in many of these studies, and there is special emphasis placed on this aspect of hydrocarbon–Pt interactions in many additional publications (55–66). There is general agreement that the stable surface species with respect to hydrogenation/decomposition is ethylidyne (44, 46, 48–51, 53–56) and that this species undergoes C–C bond scission in order to complete ethane decomposition (43, 45, 56). Other studies indicate that C–C bond scission takes place from C_2H_5 or C_2H_4 species (52, 66) or that ethylidyne dehydrogenates further prior to C–C bond scission (44).

There is considerable variation in opinion regarding the important intermediate C_2H_4 species in Pt-surface chemistry. Carter and Koel (44) and Yeo *et al.* (48) propose di-σ ethylene transforming to ethylidene ($CHCH_3$) prior to dehydrogenating to ethylidyne. Cortright *et al.* (52) also propose the di-σ intermediate, but include a possible transformation to π ethylene in the reaction pathway for ethane hydrogenolysis. De La Cruz and Sheppard (50) support ethane dehydrogenating to di-σ ethylene, which dehydrogenates directly to ethylidyne, while Newell *et al.* (51) propose ethyl dehydrogenating to ethylidene, which dehydrogenates directly to ethylidyne. Zaera *et al.* (49) propose reaction coordinates for ethyl dehydrogenating to π ethylene, which undergoes a fast and reversible transformation to di-σ ethylene prior to transforming to ethylidene, which then dehydrogenates to ethylidyne. Loaiza *et al.* (46) argue for ethane dissociative adsorption to ethyl, which dehydrogenates through di-σ ethylene to ethylidyne. These authors acknowledge that ethyl dehydrogenation through ethylidene is likely to dominate at elevated temperatures. Chen *et al.* (53) and Somorjai and Rupprechter (54) find that π ethylene is the key intermediate in ethylene hydrogenation through ethyl, which desorbs associatively to ethane.

Measured and calculated ethylene heat of adsorption is found to vary considerably in the literature. Reports for the more weakly bound π ethylene species vary from 29.3 ± 8.4 kJ/mol (58) to a calculated value of 103 kJ/mol (62), with additional experiments indicating values of 35 ± 10 (60) and 40 ± 10 kJ/mol (59). More strongly bound di-σ ethylene is found to have a heat of adsorption varying from 54.4 ± 16.7 kJ/mol (58) to a calculated value of 171 kJ/mol (62). Experiments that do not indicate a distinction between π and di-σ species report values for ethylene desorption energy of 29.3 ± 8.4 (56), 37.7 ± 8.4 (57), and 50.2 ± 13.4 (55). Spiewak *et al.* (61) report a mix of π and di-σ species with a heat of adsorption of 120 kJ/mol determined from a microcalorimetric measurement.

In light of the wide variation in reported values for ethylene heat of adsorption and the likelihood of a fast and reversible transformation between π and di-σ species (49), we do not distinguish between π and di-σ ethylene in this work and use a value of 50.2 kJ/mol for the ethylene desorption energy. This value agrees with experimental measurements in which there was no indication as to the Pt–ethylene bond structure (55) and with quasi-empirical calculations (70) from which much of the surface energetics used in (42) and described below are taken. In addition, at the high temperatures encountered in this reactor system, we assume that ethyl dehydrogenates to ethylidene (46), which can either

TABLE 1

Heterogeneous Reaction Mechanism for the Partial Oxidation of Ethane on Platinum Units: S_o [-], A [s^{-1}, K^{-n}], E_a [kJ/mol]

	Reaction		S_o or A	E_a	Reference[a]
R1	$C_2H_6 + Pt(s) + Pt(s)$	$\rightarrow C_2H_6(s)$	$S_o = 0.015$	0.0	Est. this work; (42)
R2	$C_2H_4 + Pt(s)$	$\rightarrow C_2H_4(s)$	$S_o = 0.015$	0.0	Est. this work; (42)
R3	$C_2H_2 + Pt(s)$	$\rightarrow C_2H_2(s)$	$S_o = 0.05$	0.0	Est. this work
R4	$H_2 + Pt(s) + Pt(s)$	$\rightarrow H(s) + H(s)$	$S_o = 0.046$[b]	0.0	(38)
R5	$O_2 + Pt(s) + Pt(s)$	$\rightarrow O(s) + O(s)$	$S_o = 0.07$ (300/T)	0.0	(38)
R6	$CH_4 + Pt(s) + Pt(s)$	$\rightarrow CH_3(s) + H(s)$	$S_o = 9 \times 10^{-4}$	72.0	(42)
R7	$CH_4 + O(s) + Pt(s)$	$\rightarrow CH_3(s) + OH(s)$	$1.36 \times 10^{10} \times T^{0.7}$	$42.0 + 8\theta_O$	(75); (69)
R8	$CH_4 + OH(s) + Pt(s)$	$\rightarrow CH_3(s) + H_2O(s)$	$S_o = 1.0$	10.0	Est. this work; (69)
R9	$CH_4 + C(s)$	$\rightarrow CHCH_3(s)$	$S_o = 7 \times 10^{-9}$	$23.0 + 47.5\theta_C$	Est. this work; (42)[f]
R10	$H_2O + Pt(s)$	$\rightarrow H_2O(s)$	$S_o = 0.75$	0.0	(38)
R11	$CO_2 + Pt(s)$	$\rightarrow CO_2(s)$	$S_o = 0.005$	0.0	Est. this work
R12	$CO + Pt(s)$	$\rightarrow CO(s)$	$S_o = 0.84$	0.0	(73)
R13	$C_2H_5 + Pt(s)$	$\rightarrow CH_2CH_3(s)$	$S_o = 1.0$	0.0	Est. this work
R14	$CH_3 + Pt(s)$	$\rightarrow CH_3(s)$	$S_o = 1.0$	0.0	Est. this work
R15	$H + Pt(s)$	$\rightarrow H(s)$	$S_o = 1.0$	0.0	(39)
R16	$O + Pt(s)$	$\rightarrow O(s)$	$S_o = 1.0$	0.0	(39)
R17	$OH + Pt(s)$	$\rightarrow OH(s)$	$S_o = 1.0$	0.0	(39)
R18	$C_2H_6(s)$	$\rightarrow Pt(s) + Pt(s) + C_2H_6$	1.0×10^{13}	20.9	(42)
R19	$C_2H_4(s)$	$\rightarrow Pt(s) + C_2H_4$	1.0×10^{13}	50.2	(42)
R20	$C_2H_2(s)$	$\rightarrow Pt(s) + C_2H_2$	1.0×10^{12}	58.6	This work[c]
R21	$H(s) + H(s)$	$\rightarrow Pt(s) + Pt(s) + H_2$	1.0×10^{13}	$67.4 - 10\theta_H$	(38)
R22	$O(s) + O(s)$	$\rightarrow Pt(s) + Pt(s) + O_2$	1.0×10^{13}	$227.4 - 188\theta_O$	(38)[d]
R23	$CH_3(s) + H(s)$	$\rightarrow CH_4 + Pt(s) + Pt(s)$	4.1×10^{11}	$50 - 5\theta_H$	This work; (42)[e]
R24	$CH_3(s) + OH(s)$	$\rightarrow CH_4 + O(s) + Pt(s)$	1.0×10^{13}	85.9	(69)[f]
R25	$CHCH_3(s)$	$\rightarrow CH_4 + C(s)$	1.0×10^{10}	$25.5 + 47.5\theta_C$	Est. this work; (42)[f]
R26	$CH_3(s) + H_2O(s)$	$\rightarrow CH_4 + OH(s) + Pt(s)$	1.0×10^{13}	23.0	(69)[f]
R27	$H_2O(s)$	$\rightarrow H_2O + Pt(s)$	4.5×10^{12}	41.8	(40)
R28	$CO_2(s)$	$\rightarrow CO_2 + Pt(s)$	1.0×10^{13}	27.1	[c]
R29	$CO(s)$	$\rightarrow CO + Pt(s)$	2.0×10^{16}	$146 - 33\theta_{CO}$	This work; (73)[e]
R30	$CH_2CH_3(s)$	$\rightarrow Pt(s) + C_2H_5$	1.0×10^{13}	173.0	[c]
R31	$CH_3(s)$	$\rightarrow Pt(s) + CH_3$	1.0×10^{13}	163.0	[c]
R32	$H(s)$	$\rightarrow H + Pt(s)$	6.0×10^{13}	$254.4 - 5\theta_H$	[c,e]
R33	$O(s)$	$\rightarrow O + Pt(s)$	1.0×10^{13}	$358.8 - 94\theta_O$	[c,e]
R34	$OH(s)$	$\rightarrow OH + Pt(s)$	5.0×10^{13}	$251.1 - 167\theta_O$	(41)[e]
R35	$H(s) + O(s)$	$\rightarrow OH(s) + Pt(s)$	3.5×10^{12}	11.2	(41)
R36	$OH(s) + Pt(s)$	$\rightarrow H(s) + O(s)$	2.0×10^{11}	$77.3 - 73.2\theta_O$	[c,e]
R37	$H(s) + OH(s)$	$\rightarrow H_2O(s) + Pt(s)$	5.5×10^{12}	66.2	(41)
R38	$H_2O(s) + Pt(s)$	$\rightarrow H(s) + OH(s)$	3.1×10^{10}	$101.4 + 167\theta_O$	[c,e]
R39	$OH(s) + OH(s)$	$\rightarrow H_2O(s) + O(s)$	2.0×10^{12}	74.0	(41)
R40	$H_2O(s) + O(s)$	$\rightarrow OH(s) + OH(s)$	2.7×10^{11}	$43.1 + 241\theta_O$	[c,e]
R41	$C(s) + O(s)$	$\rightarrow CO(s) + Pt(s)$	1.0×10^{11}	0.0	This work; (72)
R42	$CO(s) + Pt(s)$	$\rightarrow C(s) + O(s)$	1.0×10^{11}	$236.5 - 33\theta_{CO}$	This work; (69)[e,f]
R43	$CO(s) + O(s)$	$\rightarrow CO_2(s) + Pt(s)$	1.0×10^{11}	$117.6 - 33\theta_{CO}$	This work; (72)[g]
R44	$CO_2(s) + Pt(s)$	$\rightarrow CO(s) + O(s)$	1.0×10^{11}	$173.3 + 94\theta_O$	This work;[c,e]
R45	$CO(s) + OH(s)$	$\rightarrow CO_2(s) + H(s)$	5.4×10^{10}	$38.7 - 33\theta_{CO}$	This work; (69)[e,h]
R46	$CO_2(s) + H(s)$	$\rightarrow CO(s) + OH(s)$	5.4×10^{10}	28.3	This work; (69)[f,h]
R47	$CH_3(s) + Pt(s)$	$\rightarrow CH_2(s) + H(s)$	3.4×10^{13}	70.3	(42)
R48	$CH_2(s) + H(s)$	$\rightarrow CH_3(s) + Pt(s)$	8.4×10^{13}	$0.0 - 5\theta_H$	(42)[e]
R49	$CH_2(s) + Pt(s)$	$\rightarrow CH(s) + H(s)$	2.0×10^{14}	$58.9 + 50\theta_C$	(42)
R50	$CH(s) + H(s)$	$\rightarrow CH_2(s) + Pt(s)$	8.4×10^{13}	$0.0 - 5\theta_H$	(42)[e]
R51	$CH(s) + Pt(s)$	$\rightarrow C(s) + H(s)$	8.4×10^{13}	$0.0 - 5\theta_H$	(42)[e]
R52	$C(s) + H(s)$	$\rightarrow CH(s) + Pt(s)$	3.4×10^{13}	138.0	(42)
R53	$C_2H_6(s) + O(s)$	$\rightarrow CH_2CH_3(s) + OH(s) + Pt(s)$	1.0×10^{13}	25.1	Estimate
R54	$CH_2CH_3(s) + OH(s) + Pt(s)$	$\rightarrow C_2H_6(s) + O(s)$	1.0×10^{13}	77.4	[c]
R55	$C(s) + H_2$	$\rightarrow CH_2(s)$	$S_o = 0.04$	$29.7 + 4.6\theta_C$	(42)
R56	$CH_2(s)$	$\rightarrow C(s) + H_2$	7.69×10^{13}	$25.1 + 50\theta_C$	(42)
R57	$C_2H_6(s)$	$\rightarrow CH_2CH_3(s) + H(s)$	1.0×10^{13}	57.7	(42)
R58	$CH_2CH_3(s) + H(s)$	$\rightarrow C_2H_6(s)$	1.0×10^{13}	41.8	(42)[f]

TABLE 1—*Continued*

	Reaction		S_o or A	E_a	Reference[a]
R59	$C_2H_6(s)$	$\rightarrow CH_3(s) + CH_3(s)$	7.0×10^{12}	89.0	(42)[f]
R60	$CH_3(s) + CH_3(s)$	$\rightarrow C_2H_6(s)$	2.7×10^{12}	14.5	(42)
R61	$CH_2CH_3(s) + Pt(s)$	$\rightarrow CHCH_3(s) + H(s)$	2.7×10^{13}	54.4	(42)
R62	$CHCH_3(s) + H(s)$	$\rightarrow CH_2CH_3(s) + Pt(s)$	2.7×10^{12}	29.3	This work; (42)
R63	$C_2H_4(s)$	$\rightarrow CHCH_3(s)$	1.0×10^{13}	83.3	(42)
R64	$CHCH_3(s)$	$\rightarrow C_2H_4(s)$	1.0×10^{13}	75.3	(42)
R65	$C_2H_4(s) + Pt(s)$	$\rightarrow CHCH_2(s) + H(s)$	1.0×10^{13}	112.7	(70)[f]
R66	$CHCH_2(s) + H(s)$	$\rightarrow C_2H_4(s) + Pt(s)$	1.0×10^{13}	33.5	(70)[f]
R67	$CHCH_3(s) + Pt(s)$	$\rightarrow CCH_3(s) + H(s)$	5.4×10^{13}	99.1	This work; (42)
R68	$CCH_3(s) + H(s)$	$\rightarrow CHCH_3(s) + Pt(s)$	1.0×10^{13}	75.3	(42)
R69	$CHCH_3(s) + Pt(s)$	$\rightarrow CHCH_2(s) + H(s)$	1.0×10^{13}	128.5	(70)[f]
R70	$CHCH_2(s) + H(s)$	$\rightarrow CHCH_3(s) + Pt(s)$	1.0×10^{13}	57.3	(70)[f]
R71	$CCH_3(s) + Pt(s)$	$\rightarrow CH_3(s) + C(s)$	1.0×10^{13}	$46.9 + 50\theta_C$	(42)
R72	$CH_3(s) + C(s)$	$\rightarrow CCH_3(s) + Pt(s)$	1.0×10^{13}	46.0	(42)
R73	$CCH_3(s)$	$\rightarrow CHCH_2(s)$	1.0×10^{13}	176.0	[c]
R74	$CHCH_2(s)$	$\rightarrow CCH_3(s)$	1.0×10^{13}	128.6	[i]
R75	$CHCH_2(s) + Pt(s)$	$\rightarrow CCH_2(s) + H(s)$	1.0×10^{13}	121.3	(70)[f]
R76	$CCH_2(s) + H(s)$	$\rightarrow CHCH_2(s) + Pt(s)$	1.0×10^{13}	51.7	(70)[f]
R77	$C_2H_2(s)$	$\rightarrow CCH_2(s)$	1.0×10^{13}	61.5	This work [f,i]
R78	$CCH_2(s)$	$\rightarrow C_2H_2(s)$	1.0×10^{13}	4.2	This work [c]
R79	$C_2H_2(s) + Pt(s)$	$\rightarrow CCH(s) + H(s)$	1.0×10^{13}	133.5	(70)[f]
R80	$CCH(s) + H(s)$	$\rightarrow C_2H_2(s) + Pt(s)$	1.0×10^{13}	66.9	(70)[f]
R81	$CCH(s) + Pt(s)$	$\rightarrow CH(s) + C(s)$	1.0×10^{13}	125.1	(70)[f]
R82	$CH(s) + C(s)$	$\rightarrow CCH(s) + Pt(s)$	1.0×10^{13}	121.3	(70)

[a] The first note indicates the source for the sticking coefficient or preexponential factor. The second note is for the activation energy. If only one note appears then it is for both parameters or only for the activation energy if the preexponential factor is a nominal value.

[b] Hydrogen adsorption is modeled as first order in vacant surface sites.

[c] Activation energy is determined by thermodynamic constraints. The resulting surface energy level is consistent with well-known gas-phase species formation enthalpies.

[d] Activation energy has been modified slightly from the literature value (213 kJ/mol) so that the surface energy level is thermodynamically consistent with well-known gas-phase species formation enthalpies.

[e] Coverage dependence applied so that the reaction scheme remains thermodynamically consistent.

[f] The activation energy has been adapted from the values calculated in (69), (70), or (42) to form a thermodynamically consistent reaction scheme, which gives priority to the formation enthalpies of the gas-phase species. Procedure is as described in (42).

[g] Coverage dependence from typical literature values. For example, (74).

[h] In the absence of data for the reaction on platinum, the activation energy is estimated by analogy to reaction energetics on palladium (69).

[i] Isomerization activation barriers cannot be determined using the calculational framework in (69). Energetics are estimated.

transform to ethylene and desorb or dehydrogenate to ethylidyne. In our simulations, ethylidyne predominantly undergoes C–C bond scission, resulting in CO, CO_2, and CH_4. However, ethylidyne dehydrogenation is also modeled, which leads to small amounts of C_2H_2.

Other key features of the mechanism developed for this work are as follows:

1. Dissociative adsorption [R4, R5] and associative desorption [R20, R21] of H_2 and O_2, with a temperature-dependent sticking coefficient for O_2.

2. Dissociative adsorption of CH_4 on bare platinum sites [R6], as well as via three adsorbate assisted routes [R7–R9].

3. Reversible ethane adsorption, forming an adsorbed ethane molecule occupying two platinum sites [R1, R18], which undergoes dehydrogenation to form surface ethyl ($CH_2CH_3(s)$) either directly [R57] or by an oxygen-assisted route to form ethyl and hydroxyl [R53]. Ethyl undergoes further dehydrogenation to form ethylidene ($CHCH_3(s)$) [R59].

4. Reversible ethylene adsorption [R2, R19] followed by reversible isomerization to ethylidene [R63, R64].

5. Heterogeneous oxidation of carbon via ethylidene dehydrogenation to form ethylidyne ($CCH_3(s)$) [R67]. Ethylidyne then undergoes carbon–carbon bond scission to form methyl and surface carbon [R71]. Surface carbon oxidizes to form surface CO [R41] that can either desorb [R29] or undergo further oxidation to form surface CO_2 [R43]. Carbon dioxide may also form via CO oxidation by adsorbed OH [R45].

6. Methane desorption via recombination of adsorbed methyl with a number of surface species [R23, R24, R26] and methane gas formation via ethylidene decomposition to CH_4 and C(s) [R25]. Methyl decomposition occurs via direct, reversible dehydrogenation [R47–R52].

7. Oxidation of adsorbed hydrogen to hydroxyl [R35], which can then combine with another adsorbed hydrogen to form H_2O [R37] or disproportionate to form H_2O and O [R39]. Water is subject to reversible absorption through [R10, R27].

Species containing more than two carbon atoms are not included in either the homogeneous or the heterogeneous mechanisms, nor are there any oxygenated hydrocarbons in the heterogeneous mechanism. Experiments in which the selectivities to species containing more than two carbon atoms were measured indicate that their total selectivity is approximately 5% across the entire range of H_2 inlet feed ratios examined here [8]. In our simulations, the omission of these species leads to an overprediction of the ethylene selectivity by approximately 5% absolute selectivity. Rather than participating in chain-building steps, C_1 radicals in our simulation recombine to form C_2 species (primarily ethylene). Oxygenated species are not found experimentally under the conditions considered here [6, 8], but are found under leaner conditions burning higher alkanes [67].

Rate constants for most of the reactions used in the mechanism have been reported previously; references to these works are discussed below. However, a number of the reactions involving adsorbed carbon-containing species have not been adequately characterized. Rate constants for these reactions were adjusted to achieve agreement with the experimental data (Refs. 6 and 8). Typically, only the preexponential factor was adjusted (or the sticking coefficient in the case of adsorption reactions), since the activation energies are largely taken from the literature and form a thermodynamic scheme that is consistent with well-known gas-phase heats of formation (see below). The reactions selected for adjustments were chosen based on a sensitivity analysis (see Results). Details of these adjustments are described below. Despite the large number of reactions in the heterogeneous mechanism, there are relatively few adjustable parameters required to obtain agreement between the simulations and the experiments. Most values for kinetic parameters are either taken directly from previous reports or assigned a nominal value (1×10^{13} s^{-1} (68)) that was not adjusted.

A large portion of the surface carbon chemistry is taken directly from Wolf *et al.* (42), in which simulations are compared to oxygen-free methane conversion to ethane experiments. Of these, only the C_2H_6 and C_2H_4 sticking coefficients [R1, R2], the preexponential factors for ethane decomposition to methyl radicals [R59], reversible recombination of ethylidene and hydrogen to form ethyl [R61, R62], ethylidene dehydrogenation to ethylidyne [R67], and methyl recombination with hydrogen to form methane gas [R23] were adjusted. For all remaining reactions, the previously reported rate constants were used. Activation energies for reactions [R9, R25, R59, R60, R65, R66, R69, R70, R75, R77, R79, R80, and R81] were adjusted from the published values (42, 69, 70) to meet the constraint of thermodynamic consistency with well-established gas-phase heats of formation, using the procedure described in Ref. (42). They were not altered further to improve agreement with the data in Ref. (6).

Hydrogen oxidation on platinum has been studied extensively and several detailed mechanisms have been reported in the literature (38, 39, 71). Two key sets of experimental data with corresponding mechanisms are those reported by Rinnemo *et al.* (38) for the ignition of hydrogen/oxygen mixtures and the steady-state oxidation data of Williams *et al.* (71); both of these processes may be important in modeling chemistry in the SCTR. We find that neither mechanism can reproduce both data sets. Consequently, the hydrogen oxidation subset is taken without modification from work we have performed which resulted in a mechanism explaining both ignition and steady-state oxidation at high temperatures. That work is currently in preparation for publication. The values for the kinetic parameters used in that mechanism rely heavily on published values in the literature. Hydrogen and O_2 adsorption and desorption are from Rinnemo *et al.* (38), H_2O desorption energy is from Fisher and Gland (40), radical species treatment is from Warnatz *et al.* (39), and the surface oxidation reaction energetics are from Anton and Cadogan (41). Preexponential factors used in the mechanism are adjusted from nominal values in a fit to the Williams *et al.* (71) oxidation data. Coverage dependent desorption energies for H_2 and O_2 were fit so that the mechanism accurately predicts ignition temperature. Using this new mechanism, simulations of both H_2/O_2 ignition (38) and high-temperature steady-state hydrogen oxidation (71) are in good agreement with the published experimental data.

The carbon oxidation subset is very important for the current work and the preexponential factors for oxidation of adsorbed carbon [R41] and CO [R43, R45], as well as CO desorption [R29], are adjustable parameters in the mechanism. The energetics for the carbon and CO oxidation reactions are taken from calculations by Shustorovich and Sellers (69) and experiments by Campbell *et al.* (72). The CO desorption energy is taken from later work by Campbell *et al.* (73). For the CO dissociation reaction [R42], the activation energy was adjusted to achieve consistency with the gas-phase thermochemistry, again using the previously reported procedure (see above) (42). Data concerning the activation energies for reactions [R45] and [R46] are absent from the literature; consequently, values were estimated by analogy to the same reactions on palladium (69). The coverage dependence used for reaction [R45] is typical of values found in the literature (see, for example, Ref. 74). Finally, the calculational procedure used by Shustorovich and Sellers (69) is not applicable to the isomerization reactions [R74, R77]; consequently, the activation energies for these reactions were estimated.

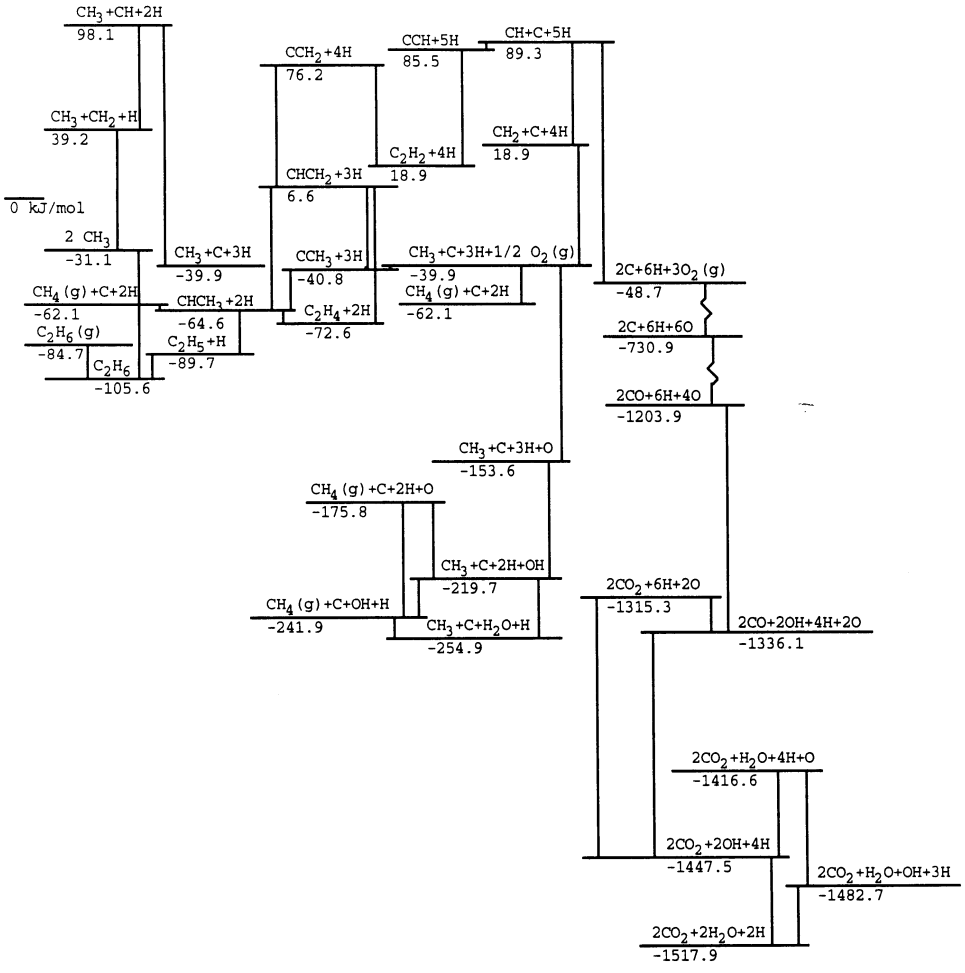

FIG. 2. Energy level diagram for the surface reactions shown in Table 1.

The energy level diagram in Fig. 2 demonstrates thermodynamic consistency among the surface reactions in Table 1. For clarity, activation barriers are not shown, only the reaction enthalpies. All energy levels are referenced to 0 kJ/mol in the gas phase at 298 K. Note that the energy for ethane gas is −84.7 kJ/mol, which is its formation enthalpy at 298 K (76). To further demonstrate thermodynamic consistency with the gas-phase heats of formation of the major species in this mechanism, we consider the desorption processes from several key energy levels in Fig. 2. From the level containing $C_2H_4 + 2H$ at −72.6 kJ/mol, we add 50.2 and 67.4 kJ/mol for the ethylene and hydrogen desorption energies, respectively. The result is 45 kJ/mol, which is only 7.5 kJ/mol below the 52.5 kJ/mol heat of formation for gas-phase ethylene (0 kJ/mol for H_2(g) at 298 K) (76). Similar analysis for the level containing $C_2H_2 + 4H$ at 18.9 kJ/mol results in 212.3 kJ/mol, which is 14.1 kJ/mol below the 226.7 kJ/mol heat of formation for gas-phase acetylene (76). Desorbing $2CO + 6H + 4O$ from the level at −1203.9 kJ/mol results in an energy deficit of 33.9 kJ/mol. A deficit of 42.2 kJ/mol arises from desorbing $2CO_2 + 2H_2O + 2H$ from the energy level at −1517.9 kJ/mol. These increasing deficits are due to the larger number of reactions involved in attaining the energy levels from which the species are desorbed, and errors in the energetics of these reactions accumulate. Nevertheless, the errors are not severe, amounting to only 3.3% of the total heat of formation for $2CO_2(g) + 2H_2O(g)$ for the case with the largest deficit. Additionally, these calculations are for species at 298 K—a lower temperature than that encountered in the reactor simulation. As the temperature increases, the gas-phase heats of formation change, but tend to have a compensating effect in the final sum (77). Taking this into account, we consider the accumulated energy errors described above insignificant.

RESULTS

Sensitivity Analysis

Our general approach to adjusting the heterogeneous chemical mechanism was to determine which reactions most strongly influence the calculated conversion and

selectivities and adjust the preexponential factor for those reactions to obtain good fits to the experimental data for an $C_2H_6:O_2=2:1$ mixture (6), and an $C_2H_6:H_2:O_2=2:2:1$ mixture (8). Figure 3 contains bar graphs of the sensitivity for ethane conversion (Fig. 3a) and ethylene (Fig. 3b) and CO (Fig. 3c) selectivities to small changes in the preexponential factor for a number of important surface reactions. Solid and open bars represent sensitivities for the $C_2H_6:O_2=2:1$, and $C_2H_6:H_2:O_2=2:2:1$ mixtures, respectively. Reactions in Table 1 that do not appear in Fig. 3 have sensitivity coefficients that fall below 0.05 under all conditions. Sensitivity coefficients are defined as (78)

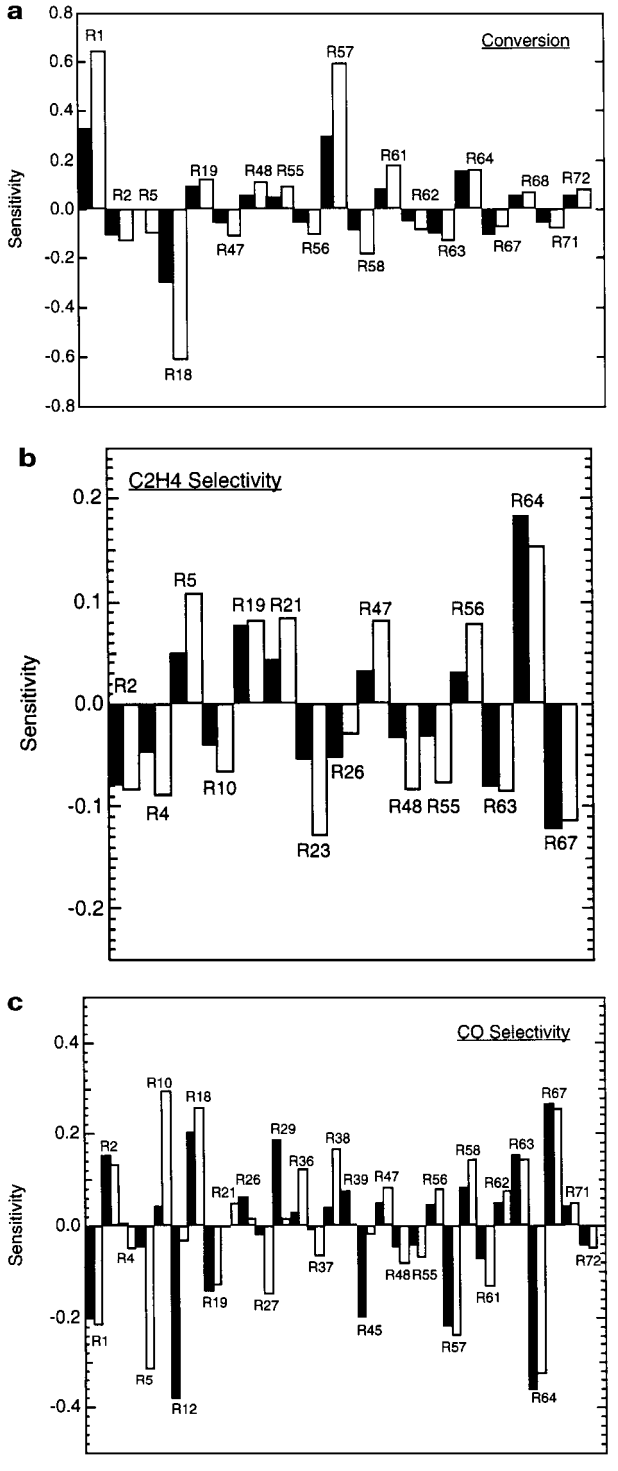

FIG. 3. Bar graphs showing the normalized sensitivity coefficients for (a) ethane conversion, (b) ethylene selectivity, and (c) CO selectivity to a number of important surface reactions.

$$S = \left(\frac{A}{x}\right)\left(\frac{\Delta x}{\Delta A}\right), \qquad [1]$$

where S is the sensitivity coefficient, A is the preexponential factor, x is the quantity in question (conversion or selectivity), and Δ indicates a small change in either A or x.

In practice, sticking coefficients for ethane and ethylene [R1, R2] were adjusted within reasonable bounds so that an approximate fit of the experimental data was achieved. These values were then not subject to further adjustment. The same is true for the ethylene–ethylidene isomerization reactions [R63, R64] (which in fact remain at nominal values), reversible CH_4 adsorption [R9, R25], and the acetylene sticking coefficient [R3] and desorption reaction [R20].

Of the remaining reactions with significant sensitivity coefficients, associative CH_4 desorption [R23], CO desorption [R29], carbon oxidation [R41 ($S < 0.05$)], CO oxidation [R43 ($S < 0.05$), R45], reversible ethyl dehydrogenation to ethylidene [R59, R60], and the ethylidene dehydrogenation [R67] are adjusted in order to fit the experimental data for the conditions discussed above. We left many parameters at their nominal values despite large sensitivities (e.g., ethylene desorption [R19]), thus minimizing the number of adjustments necessary to fit the experimental data. Note that some reactions do not have large sensitivities, yet are important to the reaction mechanism due to a large, nonrate-limiting flux through that reaction. Examples of this are CO_2 desorption [R28], carbon oxidation [R41], and methylene dehydrogenation [R49–R52]. Other reactions have low sensitivities and low fluxes, but are included in the mechanism for completeness. Examples of these are the reactions in the ethylidyne dehydrogenation pathway through acetylene and eventually complete decomposition [R73–R82]. Other reactions are included in the mechanism in order to demonstrate their *lack* of importance, such as the H, O, and OH radical desorption reactions [R30–R34]. These radical desorption reactions will be addressed specifically in the discussion to follow in a later section.

It is clear that any number of combinations of adjustments to these reaction parameters could lead to a fit of the experimental data. Therefore we do not propose that the mechanism in Table 1 is unique or complete in its description of ethane oxidative surface chemistry, but rather represents a reasonable model of the chemical phenomena associated with ethane conversion to ethylene in SCTRs.

Ethane, Oxygen, Nitrogen Mixtures

The basic experiment to which we compare our simulations involves the reaction of ethane and O_2 with a N_2 diluent in a SCTR. The experimental results were published by Bodke *et al.* (6). Briefly, the experimental reactor consisted of an α-alumina (92% Al_2O_3, 8% SiO_2) monolith with 45 ppi coated with 1% Pt by weight. The total flow rate into the reactor was 5 slpm. The reactor pressure was 1.2 atm. The N_2 mole fraction was always 30%, with the $C_2H_6 : O_2$ mole-fraction ratio ranging from 1.5 to 2.1. Error bars are not shown for the Bodke *et al.* data (6), but it is stated that gas-phase carbon and hydrogen balances closed to within ±5%. The schematic shown in Fig. 1 typifies the basic reactor geometry used in all SCTR experiments we consider.

The fit between the data of Bodke *et al.* (6) and our simulations is quite good for all measured quantities, supporting the validity of our chemical and transport models. The charts in Fig. 4 compare model predictions with the experimental results of Bodke *et al.* (6) for ethane conversion, ethylene and CO selectivities, and reactor exit temperature. Results in Fig. 4a show that in both the experiments and the simulations, ethane conversion decreases from approximately 95 to 65%, as the reactant mixture becomes more ethane-rich. The measured selectivity to ethylene increases from 57 to almost 65%; the simulations exhibit the same trend, with ~5% absolute overprediction of the selectivity. The measured selectivity to CO (Fig. 4b) decreases with increasing ethane content, dropping from near 25% to just over 15%, and the simulations fit both the trend and the absolute values well, with a tendency to overpredict selectivity for mixtures rich in ethane. Selectivities to CO_2, CH_4, H_2, and H_2O are not reported by Bodke *et al.* (6). The model predictions in Figs. 4b and 4c indicate that as the mixture becomes richer in ethane, the CO_2 and H_2 selectivities increase, while the H_2O selectivity decreases, and the CH_4 selectivity remains nearly constant. The measured selectivity to acetylene is also is not given, but the model predicts that it is always quite low (the highest selectivity to acetylene predicted by our simulations is 3.4%, corresponding to the leanest mixture considered). Finally, in both the experiments (6) and our simulations, the temperature decreases as the ethane/oxygen ratio increases (Fig. 4d). The simulations tend to overpredict temperature under richer conditions. Although the experimental uncertainty in the temperature measurement is not given (6), ±50 K does not seem unreasonable for thermocouple measurements in general. In Fig. 4d we also show the peak reactor temperature predicted by the model; the results indicate that this value exceeds the exit temperature by 50–70 K across the entire range of mixtures.

The predicted contributions of homogeneous and heterogeneous processes to the consumption of ethane and oxygen and to the formation of product species are shown in Fig. 5. Contributions are found by integrating the total molar reaction rate for each species over the reactor volume (homogeneous) or surface area (heterogeneous).

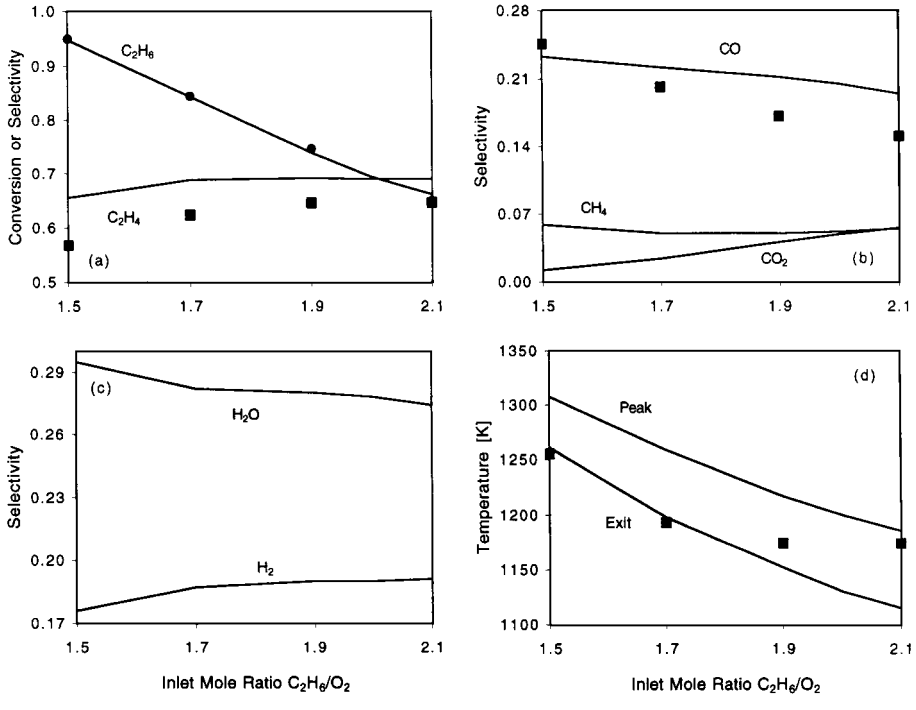

FIG. 4. Simulation results (lines) compared to experimental data (symbols) of Bodke *et al.* (6). (a) Ethane conversion and ethylene selectivity, (b) minor species carbon-atom selectivities, (c) water and H_2 selectivities, (d) reactor peak and exit temperatures.

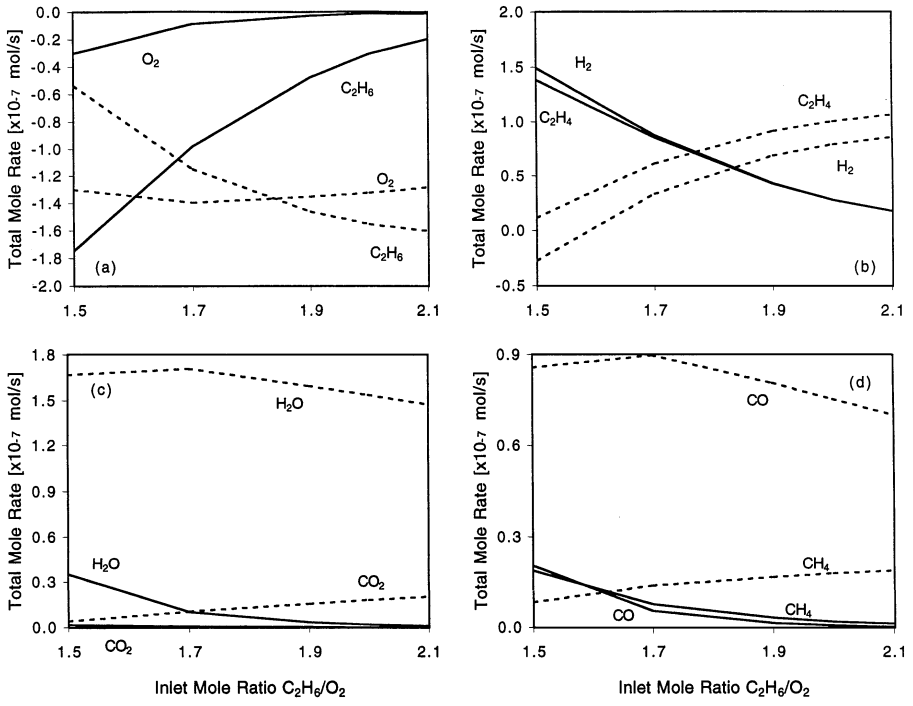

FIG. 5. Calculated contributions to the consumption or production of species from homogeneous (solid lines) and heterogeneous (dashed lines) processes.

Both processes are shown to dominate different aspects of SCTR behavior with different inlet feed compositions, indicating the importance of including both of these components of the chemistry in the mechanism. The results in Fig. 5a show that most of the ethane is consumed (i.e., a negative total molar rate of production) by homogeneous processes for the leanest mixture considered, with 76% of the converted ethane consumed by gas-phase reactions. For the richest mixture, heterogeneous ethane consumption exceeds homogeneous consumption, with only 11% of the ethane conversion occurring homogeneously. For oxygen, the heterogeneous process always dominates, and under the richest conditions nearly all of the oxygen is consumed on the surface.

A key prediction of the model is that the stoichiometric pyrolysis products ethylene and H_2 are produced almost exclusively by homogeneous processes for the leanest mixtures (Fig. 5b). In fact, the surface is a net consumer of H_2 under this lean condition. However, as the mixture becomes richer in ethane, homogeneous production of ethylene and H_2 decreases to small values, while the surface becomes a net producer of both H_2 and ethylene. For the mixture richest in ethane, only 14% of the ethylene is produced homogeneously (compared to >92% for the leanest mixture). We note that production of C_2H_2 is small under all conditions reported here. Homogeneous processes are net producers of this species, while heterogeneous processes are net consumers under leaner conditions. The highest homogeneous C_2H_2 production rate occurs at the leanest mixture, a condition for which the gas-phase temperature is also the highest.

In contrast, the simulations show that for the oxidation products CO, CO_2, and H_2O, heterogeneous production of these species is always greater than homogeneous production (Figs. 5c and 5d). (The only exception to this trend is for CH_4 at the leanest mixture. In this case both contributions are small.) The dominance of heterogeneous oxidation is greatest when the mixture is richest in ethane, a condition for which nearly all of the oxygen is consumed on the surface. The greatest shift from homogeneous to heterogeneous oxidation occurs when the C_2H_6 : O_2 mole ratio is increased from 1.5 to 1.7. This coincides with a shift to conditions resulting in the greatest increase in ethylene selectivity (Fig. 4a).

A clear picture of the heat release and total homogeneous chemical activity in the SCTR can be obtained from two-dimensional contour plots. In Fig. 6 we show such plots of temperature and total reaction rate resulting from a simulation with a C_2H_6 : O_2 mole ratio of 2.0. The total reaction rate is the net result of all homogeneous processes involving a particular gas-phase species. The temperature contours are bounded at the low end by 810 K, which is the lowest wall temperature found in this simulation. Temperatures near the inlet actually fall below this level, and this relatively small region is shown in white.

The plot in Fig. 6 shows that the highest temperature is found on the wall less than 1 mm past the start of the

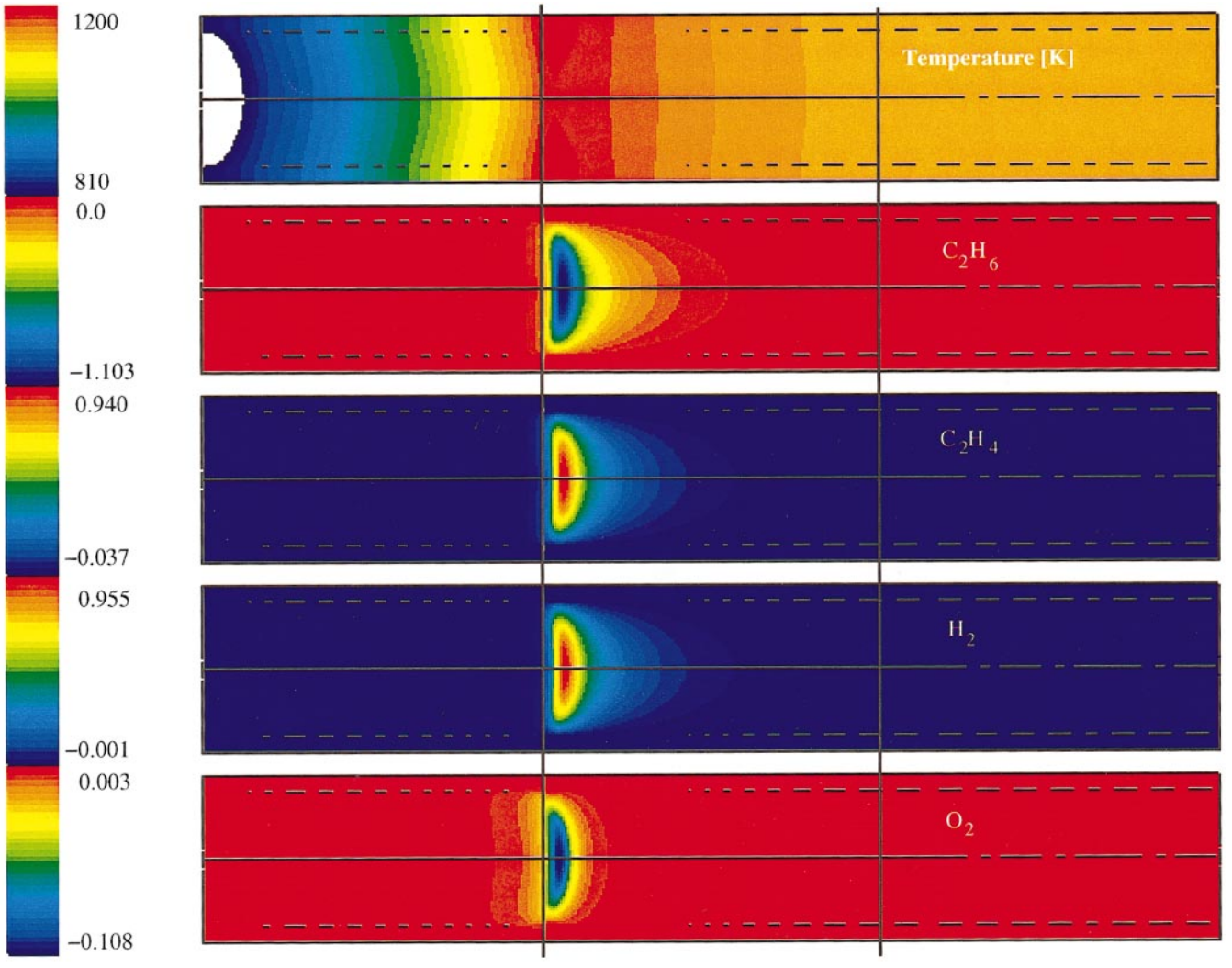

FIG. 6. Contour plots of calculated temperature [K] and total homogeneous molar reaction rates [kmol/s m^3] for selected species. The gases flow from left to right in the axisymmetric reactor tube geometry. Reactor walls are indicated by the dashed horizontal lines, and the monolith sections are separated by solid vertical lines. The radial scale has been expanded by a factor of 8.

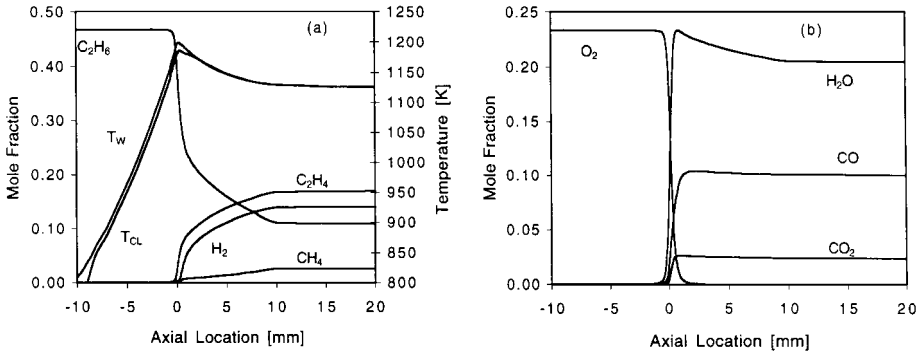

FIG. 7. Calculated axial profiles of temperature and selected species mole fractions. (a) Temperature (wall and centerline), ethane, and pyrolysis products, (b) oxygen and oxidation products. Species profiles are taken along the centerline. $C_2H_6 : O_2 = 2.0$.

catalytic section. The difference between the peak wall temperature and the gas temperature immediately adjacent to the wall is less than 1 K. At this point, the temperature on the centerline is lower than the wall temperature by approximately 14 K. As expected, total homogeneous reaction rates are greatest at the axial location where the temperature is the highest. Note, however, that rates tend to peak near the centerline and decrease in the direction of the wall at this axial location. Also note the rapid decrease in reaction rates as the temperature decreases downstream. The maximum total rate of homogeneous ethane consumption is quite high compared to the peak total rate of homogeneous oxygen consumption. Likewise, the total homogeneous rates of ethylene and H_2 production are high compared to the total production rates of the oxidation products H_2O, CO, and CO_2 (not shown).

Axial gas-phase concentration profiles in Fig. 7 make clear that O_2 is rapidly consumed within the first 1 mm of the catalytic section (which starts at the 0-mm mark) with concomitant production of the oxidation products H_2O, CO, and CO_2 (Fig. 7b). Ethane is consumed over a more extended region of the reactor, with ethylene and H_2 mole fractions increasing within the same region (Fig. 7a). These plots are illustrative of the behavior across the range of $C_2H_6 : O_2$ ratios examined. Importantly, there is essentially no oxygen in the gas phase beyond ~1.5 mm. The wall temperature is shown to be greater than the centerline temperature by approximately 10–15 K near the front of the reactor, with the greatest difference exhibited just downstream of the 0-mm mark.

The importance of gas-phase chemistry is illustrated in Fig. 8, which contains plots of the centerline rates of the dominant homogeneous reactions for the conditions represented in Figs. 6 and 7. Ethane decomposition is initiated by hydrogen-atom attack to form an ethyl radical (C_2H_5) and H_2. This radical then thermally decomposes to form ethylene and a hydrogen atom. The net forward rates of these two reactions are almost identical. Ethane is also attacked by other radicals that form at these temperatures, such as OH, CH_3, and O, but the rates of these reactions are considerably lower. Ethyl radical attack by O_2 in the gas phase, resulting in ethylene and HO_2, also occurs, but at a relatively low rate. Both reaction rates shown in Fig. 8 reach their peak approximately 1 mm from the start of the catalytic section.

The sequential nature of the heterogeneous chemistry is more clearly seen in Fig. 9, which contains axial profiles of important heterogeneous reaction rates and surface coverages. Initially, carbon and hydrogen oxidation reactions occur rapidly (Fig. 9a); however, these rates peak within 0.2 mm from the start of the catalytic section and then decrease sharply downstream of this point. At the same time, there is a dramatic decrease in the surface O coverage fraction (Fig. 9b), while the C and H coverage fractions increase. Reaction rates plotted in Fig. 9c show that the rate of O_2 adsorption is high over the first 0.2 mm of the reactor and then drops to zero. The rapid oxidation rates in the upstream portion of the reactor (Fig. 9a) coincide with high desorption rates for the oxidized species H_2O and CO, with a lag in the CO_2 desorption as the CO surface coverage

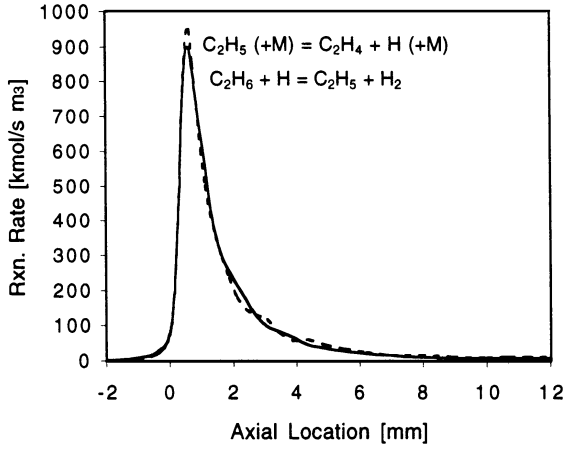

FIG. 8. Calculated reaction rates for the dominant homogenous reactions. Values are taken along the monolith channel centerline.

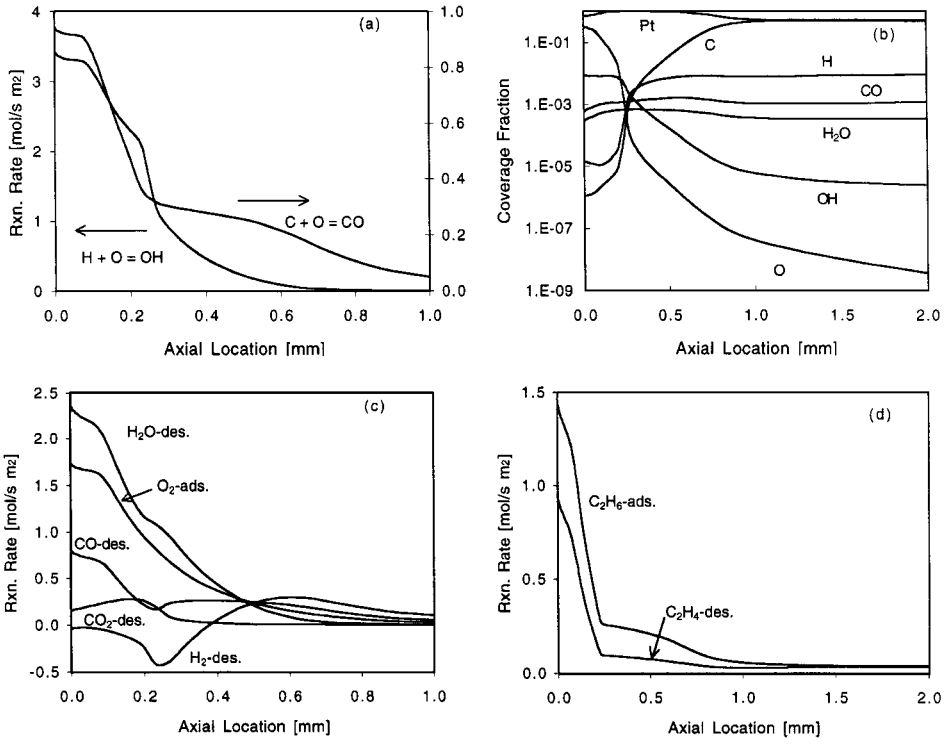

FIG. 9. Calculated surface coverages and heterogeneous reaction rates. (a) Surface carbon (right-hand ordinate) and hydrogen (left-hand ordinate) oxidation rates, (b) selected surface species coverage fractions, (c) oxygen adsorption and oxidized species desorption rates, (d) ethane adsorption and ethylene desorption rates.

increases (Figs. 9c and 9b). These desorption processes then drop to near, or just below, zero (i.e., a small net adsorption) in the remaining portion of the reactor. Hydrogen undergoes net adsorption in the first 0.3 mm (shown as negative desorption in the figure) and then undergoes net desorption in the absence of O_2 for the remainder of the reactor length. Beyond this point, both H_2 and CO undergo net desorption in the absence of O_2 for the remainder of the reactor length. In Fig. 9d we show that C_2H_6 adsorption is highest over the first 0.2 mm of the catalytic section, driven by the O-assisted surface dehydrogenation reaction [R53 in Table 1]. Ethylene desorption is also highest in this front portion of the catalytic section and exhibits a net desorption over the entire downstream portion of the reactor.

Mixtures with Hydrogen Addition

Bodke *et al.* demonstrated (8) that the addition of H_2 to the inlet feed of ethane SCTRs increases the selectivity to ethylene while maintaining high ethane conversion over platinum. The effect of H_2 addition was found to be even more dramatic on a platinum–tin alloy catalyst. In the experiments, H_2 was mixed with the inlet gases (C_2H_6, O_2, and N_2) while the mass-flow rates of ethane and O_2 were held constant (8). The total flow rate was held at 5 slpm; thus, as the H_2 mole fraction increased, the amount of N_2 dilution was decreased. We applied our models to the hydrogen addition experimental configuration, and in Fig. 10 we compare the results of our simulations with the results of the experiments by Bodke *et al.* (8).

In Fig. 10a we show that predicted ethylene selectivity is in very good agreement with the measured values. As discussed above, there is an overprediction of ~5% absolute selectivity to ethylene "built in" to our model. The predicted ethane conversion is also in very good agreement with the measured values for $H_2 : O_2$ ratios up to 1.0; the agreement is still quite satisfactory as the $H_2 : O_2$ ratio increases to 3.0, where there is an overprediction by 10% absolute conversion, or ~15% relative error. However, the trend toward decreasing conversion is reproduced. In Fig. 10b we see that measured selectivities to CO and CO_2 decrease with increasing H_2 content and the simulations reproduce these data very well. Note that there is a particularly sharp decrease in the CO_2 selectivity. Measured and predicted selectivities to CH_4 both show an increase with increasing H_2 content. The maximum deviation between the predictions and the experiments in Fig. 10b is 2.2% absolute selectivity for CH_4 at a $H_2 : O_2$ ratio of 3.0. Finally, the peak temperature in the reactor (not shown in Fig. 10) exhibits a sharp increase from 1200 to 1228 K as hydrogen is added to the feed.

To illustrate the relative contributions of homogeneous and heterogeneous processes to the consumption and

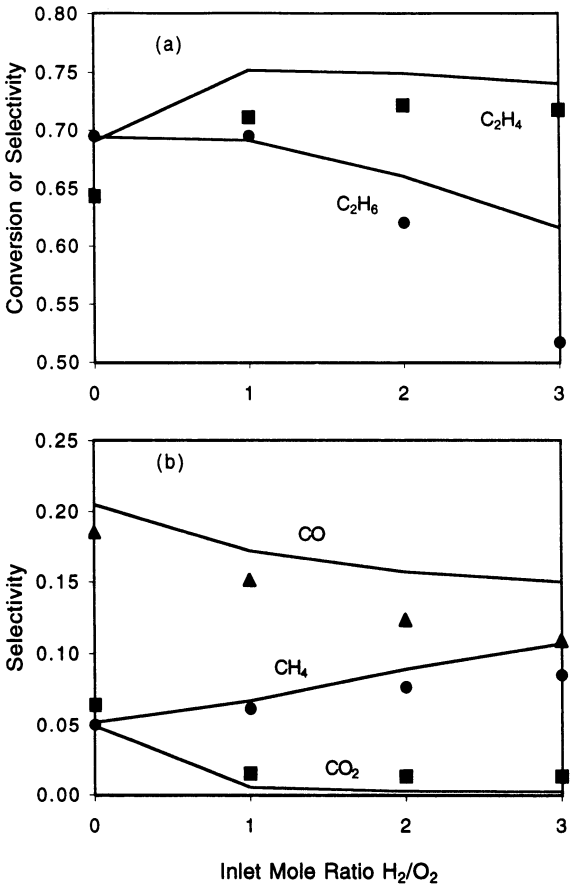

FIG. 10. Simulation results (lines) compared to the experimental data (symbols) of Bodke *et al.* (8) with H_2 addition to the inlet feed. (a) Ethane conversion and ethylene (and higher hydrocarbon) selectivities, (b) CO, CO_2, and CH_4 selectivities.

production of various gas-phase species, plots of these are shown in Fig. 11 for an inlet $C_2H_6 : O_2$ ratio of 2.0. In Fig. 11a we show that as the inlet H_2 fraction increases, the homogeneous consumption of C_2H_6 also increases significantly (i.e., a more negative total mole rate), while the heterogeneous consumption decreases (i.e., a less negative total mole rate). The homogeneous consumption rate of O_2 is always quite low under these conditions. Increasing the $H_2 : O_2$ inlet ratio from zero to one results in doubling the rate of homogeneous C_2H_4 production, as shown in Fig. 11b. The heterogeneous contribution to the C_2H_4 production rate decreases over this range. From the data in Fig. 11c we see that homogeneous production of H_2O is nearly zero at all H_2 inlet ratios, while the heterogeneous production increases steadily. Most importantly, heterogeneous contributions to the oxidation of surface carbon decrease significantly as the inlet H_2 concentration increases. In particular, heterogeneous production of CO decreases steadily with increasing H_2 (Fig. 11d), while production of CO_2 falls to nearly zero with an inlet $H_2 : O_2$ ratio of 1 : 1 (Fig. 11c).

The on-axis mole-fraction profiles produced by our simulation are shown in Fig. 12, along with several heterogeneous reaction-rate profiles and the surface coverage fractions, for a $C_2H_6 : H_2 : O_2$ ratio of 2 : 1 : 1. Similar to the profile in Fig. 7, the O_2 mole fraction profile in Fig. 12b exhibits a steep slope in the axial direction, with most of the O_2 consumed within the first 1 mm of the catalytic reactor section. The H_2 in the inlet feed is rapidly consumed at the start of the catalytic section and then returns to nearly its inlet value at the downstream end of the reactor (Fig. 12a). Unlike the case without added H_2, the O coverage on the surface is never very large (Fig. 12c). The very rapid consumption of added H_2 and the smaller amount of O coverage suggest a strong preferential oxidation of the added H_2. Surface reaction rates confirm that adsorbed H is rapidly converted (through OH) to H_2O, which then desorbs (Fig. 12d). Hydrogen exhibits a net adsorption (shown as a negative desorption rate) throughout the reactor length, and the net H_2O desorption profile is nearly a mirror image of the H_2 adsorption profile. The net O_2 adsorption rate is approximately half of the net H_2 adsorption and H_2O desorption rates throughout most of the reactor length, supporting the idea that added H_2 is preferentially oxidized to H_2O. Consistent with this is the observation that the heterogeneous reaction rate for surface C oxidation is significantly reduced in this case (Fig. 12d, compared to Fig. 9a), and the rate of heterogeneous CO oxidation is near zero (not shown).

DISCUSSION

Our simulations indicate that the fundamental chemical processes driving the performance of ethane SCTRs can be summarized as heterogeneous production of CO, CO_2, and H_2O by oxidation of surface carbon and hydrogen, coupled to both homogeneous *and* heterogeneous dehydrogenation of ethane to produce ethylene and H_2. These processes are represented schematically in Fig. 13. Surface carbon forms as a result of ethane adsorption and decomposition, while surface hydrogen can result from either ethane adsorption/decomposition or H_2 dissociative adsorption. Heat is released near the front of the reactor by heterogeneous oxidation of hydrogen and carbon, and the temperature reaches its maximum in this region. This process drives the endothermic gas- and surface-phase dehydrogenation of ethane to produce ethylene and H_2. In the downstream portion of the reactor, steam reforming of adsorbed ethane results in an additional minor heterogeneous production of H_2, CO, and CH_4. Both homogeneous and heterogeneous processes are important to the performance of this reactor and we discuss this conclusion in detail in this section.

Ethane, Oxygen, Nitrogen Mixtures

The results shown in Fig. 4 indicate a very good fit between our model and the experimental data. Our

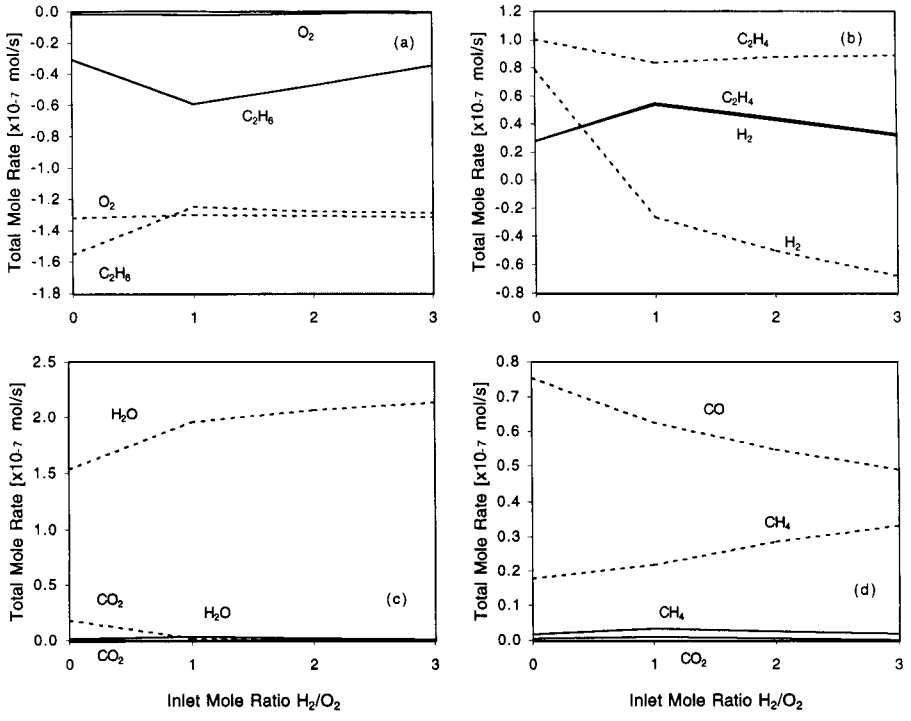

FIG. 11. Calculated contributions to the consumption or production of species from homogeneous (solid lines) and heterogeneous (dashed lines) processes. H_2 is added to the inlet feed.

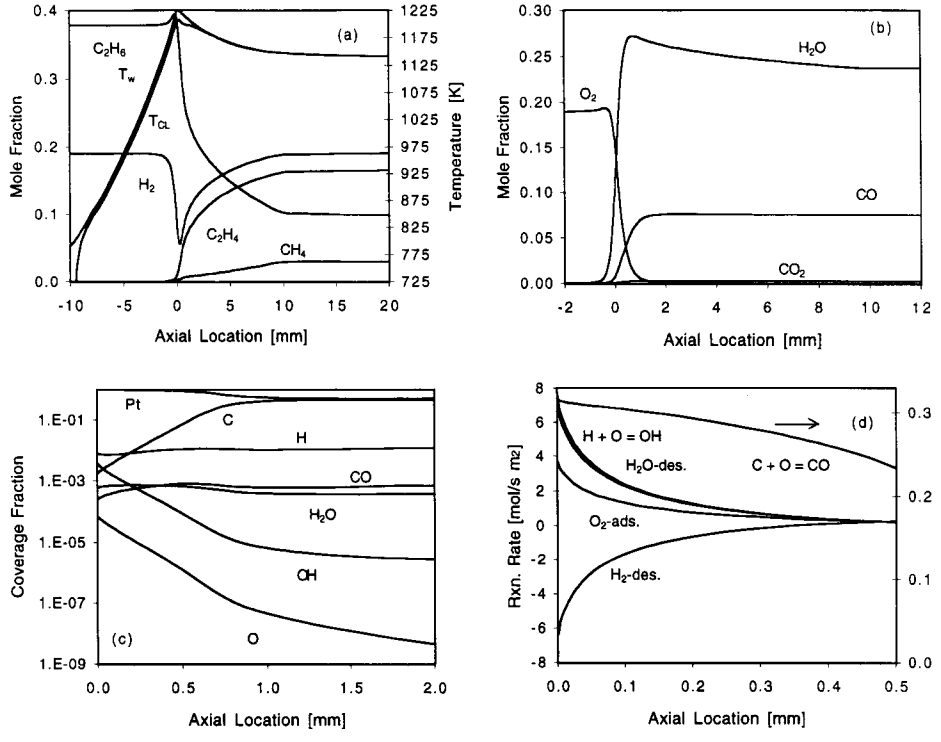

FIG. 12. (a) and (b) Calculated axial profiles of temperature and selected species mole fractions. (a) Temperature (wall and centerline), ethane, and pyrolysis products, (b) oxygen and oxidation products. (c) and (d) Calculated surface coverage fractions and selected heterogeneous reaction rates.

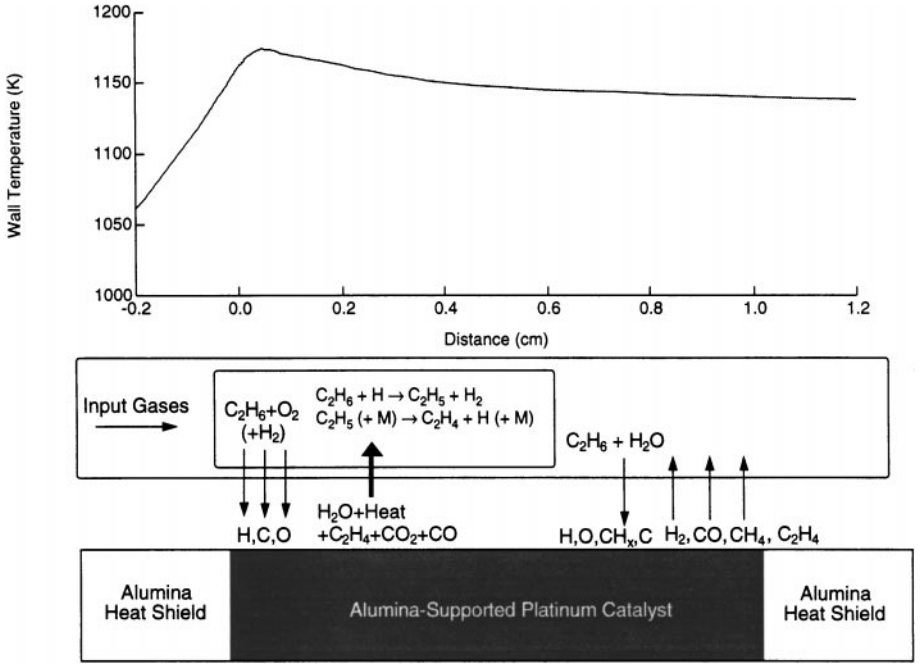

FIG. 13. Schematic representation of important heterogeneous and homogeneous processes and the reactor wall temperature.

simulations indicate that reactor performance is driven by heterogeneous oxidation processes, which release heat and facilitate homogeneous and heterogeneous pyrolysis of ethane to ethylene and H_2. Both the experiments (6) and the simulations show a maximum ethylene yield at a $C_2H_6 : O_2$ ratio of 1.5. Under this condition the results in Fig. 5 show that homogeneous chemistry dominates ethane consumption and ethylene production. However, both experiments and simulations indicate that ethylene selectivity is maximized at $C_2H_6 : O_2$ ratios of 1.7–1.9 (Fig. 3). Under these conditions, the homogeneous and heterogeneous contributions to ethane consumption and ethylene production are more competitive. The primary effect of increasing the $C_2H_6 : O_2$ ratio from 1.5 to 1.7 is to increase heterogeneous oxidation rates relative to the analogous homogeneous rates.

The results in Fig. 8 show that the key gas-phase processes are (endothermic) pyrolysis of C_2H_6, while the most important surface processes (Fig. 9) are exothermic oxidation of hydrogen and carbon. At $C_2H_6 : O_2$ ratios greater than 1.5, the ethylene yield diminishes as the reactor temperature drops and the homogeneous contribution to the ethane consumption decreases, resulting in substantially lower conversion. However, homogeneous oxidation becomes very small as the mixture becomes richer in ethane, so that the ethylene selectivity remains high.

If the goal is to maximize ethylene selectivity, then our results indicate that it is vital that oxidation processes occur heterogeneously rather than in the gas phase. In contrast, ethylene formation should occur homogeneously; this decreases the likelihood of carbon oxidation on the surface and thus increases ethylene selectivity. This is because the platinum-coated surface tends to catalyze C–C bond scission ($E_a = 89$ kJ/mol [R59], $E_a = 46.9$ kJ/mol [R71]), while the gas-phase ethane C–C bond scission has a very high activation energy (372 kJ/mol). Only when the temperature is very high, as in the leanest mixtures reported here, do the simulations predict that a significant amount of homogeneous carbon oxidation occurs. The ideal situation can therefore be characterized as heterogeneous *hydrogen* oxidation, which provides heat, coupled to homogeneous ethane dehydrogenation, which produces ethylene but not CO or CO_2.

Our results indicate that the reactor walls perform two competing functions. First, exothermic heterogeneous reactions producing H_2O, CO, and CO_2 provide heat that drives reactions in the gas phase. This is readily evident from the contour plots in Fig. 6, which show a region of lower temperature in the gas phase adjacent to the location of the highest wall temperature, i.e., a radial temperature gradient exists between the wall and the centerline gas. The region of maximum homogeneous ethane consumption, as well as ethylene and H_2 production, coincides exactly with this region of suppressed temperature. The largest difference between the wall temperature and the reactor centerline temperature occurs at the location of maximum wall temperature (Fig. 7). Production of ethylene via the very important and endothermic (ΔH° (298 K) = 146 kJ/mol) ethyl decomposition reaction (Fig. 8) reaches its maximum at this location. This is an indication that the nonuniform

wall-temperature profile plays an important role in determining the homogeneous contribution to the overall process and that inclusion of full heat transport in the wall is essential to the accurate simulation of SCTR performance.

The second function of the walls is to adsorb gas-phase H-atom radicals, thereby quenching homogeneous H-atom attack on ethane near the walls. This is suggested by the observation (Fig. 6) that total homogeneous reaction rates for the production of ethylene and other species decrease near the wall. To support this speculation, we modified our heterogeneous chemical mechanism so that adsorption of H, O, and OH radicals was not permitted. A simulation performed under this condition showed increases in conversion (+3% absolute) and ethylene selectivity (+1% absolute) and a decrease in CO selectivity (−1% absolute). These changes are associated with a 60% relative increase in the homogeneous pyrolysis rate brought about by a decrease in near-wall quenching. We performed another simulation in which desorption of radical species from the wall was prohibited. This resulted in no difference in either the calculated conversion and selectivities or the relative contributions of the homogeneous and heterogeneous processes to the reactor performance.

Experiments (6) that probe the effect of reactor monolith pore size indicate that there is virtually no difference in the ethane conversion using monoliths with 20, 45, and 80 ppi and only minor differences in the ethylene and CO selectivities. This is consistent with the idea that the presence of the wall both enhances reactor performance through intimate heat release and diminishes it through radical-species quenching. We speculate that these competing processes balance to produce practically no change in reactor performance using different monolith pore sizes. Of course, this simplified view of the pore-size effect is complicated by reactant and product mass-transfer processes that can be strongly influenced by the proximity of the wall. These issues are being addressed in ongoing research.

Mixtures with Hydrogen Addition

Evidence that heterogeneous hydrogen oxidation releases the heat necessary for homogeneous and heterogeneous ethane dehydrogenation and improved reactor performance is provided by our simulations of the hydrogen-addition experiments (8). These simulations indicate that the addition of H_2 to the inlet feed results in enhanced heterogeneous oxidation of hydrogen at the expense of carbon oxidation. In Fig. 10 we show very good agreement between the measured and calculated ethane conversion and product selectivities. Upon increasing the inlet $H_2:O_2$ ratio from zero to 1, there is a sharp decrease in the CO and CO_2 selectivities and an increase in the ethylene selectivity, while the ethane conversion remains constant. This is consistent with the results in Figs. 11c and 11d, which show that the heterogeneous oxidation of carbon to form CO and CO_2 decreases with H_2 addition. In contrast, heterogeneous production of H_2O increases substantially with H_2 addition, (Fig. 11c) while homogeneous production remains constant (and near zero). In fact, the results in Fig. 12d show that net H_2 adsorption and net H_2O desorption rates are almost perfect mirror images of each other. Reactant H_2 is consumed quickly; results in Fig. 12a show that the H_2 mole fraction decreases rapidly before recovering to a high value at the reactor exit. This type of reactor behavior is consistent with the speculation of Bodke *et al.* (8), where it is referred to as a "two-zone model." It is thus evident that reactant H_2 is almost completely oxidized heterogeneously at the start of the reactor catalytic section. Coincident with this oxidation is the release of a great deal of heat that is transferred to the gas phase, resulting from the overall exothermicity of the reaction $H_2 + 1/2\ O_2 \leftrightarrow H_2O$ (−241.8 kJ/mol).

The discussion of $C_2H_6:O_2$ mixtures above indicates that homogeneous pyrolysis promotes high ethylene yields, while dominant heterogeneous oxidation leads to maximum ethylene selectivity. The results for mixtures with H_2 in the feed are consistent with these observations and lead to another condition that enhances ethylene selectivity. Both experiments (8) and our simulations indicate an increase in the ethylene yield as the $H_2:O_2$ feed ratio increases from zero to 1 (Fig. 10a). This change in the composition at the inlet also leads to the greatest increase in homogeneous consumption of ethane and production of ethylene and H_2 (Figs. 11a and 11b). Concomitant with these changes is the large increase in heterogeneous production of H_2O, which occurs at the expense of surface-carbon oxidation, resulting in decreased CO and CO_2 selectivity and increased selectivity to ethylene. The highest measured ethylene selectivity reported (8) occurs at a feed mixture of $C_2H_6:H_2:O_2 = 2:2:1$ (Fig. 10a). Under these conditions our simulations indicate a near absence of homogeneous oxidation processes, a substantial fraction of ethane pyrolysis occurring in the gas phase, and preferential oxidation of surface hydrogen at the expense of surface carbon.

CONCLUSIONS

Our simulations indicate that the observed performance of the ethane SCTR is the result of coupled heterogeneous and homogeneous chemical processes. The valuable ethylene product of this reactor results from both homogeneous *and* heterogeneous dehydrogenation of ethane, the relative contributions of each depending on the reactor conditions. Heat is required to drive this highly endothermic dehydrogenation. We conclude that this heat is provided through heterogeneous oxidation reactions that occur very near the front of the catalytic section of the reactor. Conditions that result in optimum reactor performance are most strongly characterized by a picture of heterogeneous oxidation in

conjunction with a relatively large contribution from homogeneous ethane dehydrogenation.

The addition of H_2 to the inlet feed of this reactor results in surface hydrogen oxidation at the expense of surface carbon oxidation, producing even more highly localized heat release into the gas phase. Homogeneous ethane dehydrogenation is also enhanced, while heterogeneous decomposition and oxidation to CO and CO_2 is diminished. The selectivity to ethylene increases because selectivity to CO and CO_2 is decreased.

Radical species desorption does not play an important role in the initiation of homogeneous reactions under the conditions studied here. Localized heat release and high peak temperatures in the reactor are responsible for the short residence times required to initiate the homogeneous chemistry vital to the reactor performance. As such, it is important to incorporate full heat and mass transport in an ethane SCTR simulation in order to capture the spatial distribution of homogeneous reactions and an accurate wall temperature profile.

While we believe that this research has shed considerable light on the chemical processes relevant to the performance of ethane SCTRs, we recognize that chemical mechanisms based on a limited set of experimental data can be neither unique nor complete in their description of the detailed kinetics. More experiments and kinetic mechanism development are required to achieve a comprehensive set of rate constants. Examples include partial oxidation of methane at short contact times, ignition and high-temperature catalytic combustion of CO, and catalytic processes involving acetylene.

ACKNOWLEDGMENTS

We thank Mark Paffett of Los Alamos National Laboratory, Professor Lanny Schmidt, and Professor J. Warnatz for their technical advice. We acknowledge the Dow Chemical Company for their collaboration in this research and the Department of Energy's Office of Industrial Technologies for providing financial support.

REFERENCES

1. Huff, M., and Schmidt, L. D., *J. Phys. Chem.* **77**, 11815 (1993).
2. Dietz, A. G., and Schmidt, L. D., *Catal. Lett.* **33**, 15 (1995).
3. Yokoyama, C., Bharadwaj, S. S., and Schmidt, L. D., *Catal. Lett.* **38**, 181 (1996).
4. Witt, P. M., and Schmidt, L. D., *J. Catal.* **163**, 465 (1996).
5. Flick, D. W., and Huff, M. C., *Catal. Lett.* **47**, 91 (1997).
6. Bodke, A. S., Bharadwaj, S. S., and Schmidt, *J. Catal.* **179**, 138 (1998).
7. Bodke, A. S., Olschki, D. A., Schmidt, L. D., and Ranzi, E., *Science* **285**, 712 (1999).
8. Bodke, A. S., Henning, D., Schmidt, L. D., Bharadwaj, S. S., Maj, J. J., and Siddall, J., *J. Catal.* **191**, 62 (2000).
9. Flick, D. W., and Huff, M. C., *J. Catal.* **178**, 315 (1998).
10. Lødeng, R., Lindvåg, O. A., Kvisle, S., Reier-Nielson, H., and Holmen, A., *Appl. Catal. A* **187**, 25 (1999).
11. Flick, D. W., and Huff, M. C., *Appl. Catal. A* **187**, 13 (1999).
12. Morales, E., and Lunsford, J. H., *J. Catal.* **118**, 255 (1989).
13. Martin, G. A., Bates, A., DuCarme, V., and Mirodatos, C., *Appl. Catal.* **47**, 287 (1989).
14. Burch, R., and Crabb, E. M., *Appl. Catal. A* **97**, 49 (1999).
15. Baerns, M., and Buyevskaya, O., *Catal. Today* **45**, 13 (1998).
16. Beretta, A., Groppi, G., Majocchi, L., and Forzatti, P., *Appl. Catal. A* **187**, 49 (1999).
17. Beretta, A., Piovesan, L., and Forzatti, P., *J. Catal.* **184**, 455 (1999).
18. Beretta, A., Forzatti, P., and Ranzi, E., *J. Catal.* **184**, 469 (1999).
19. Hickman, D. A., and Schmidt, L. D., *AIChE J.* **39**, 1164 (1993).
20. Huff, M. C., and Schmidt, L. D., *AIChE J.* **42**, 3483 (1996).
21. Wolf, D., Höhenberger, M., and Baerns, M., *Ind. Eng. Chem. Res.* **36**, 3345 (1997).
22. Veser, G., and Frauhammer, J., *Chem. Eng. Sci.* **55**, 2271 (2000).
23. Deutschmann, O., and Schmidt, L. D., *Proc. Combust. Inst.* **27**, 2283 (1998).
24. FLUENT 4.5, copyright Fluent Inc., Lebanon, NH, 1999.
25. Deutschmann, O., and Schmidt, L. D., *AIChE J.* **44**, 2465 (1999).
26. Huff, M. C., Androulakis, I. P., Sinfelt, J. H., and Reyes, S. C., *J. Catal.* **191**, 46 (2000).
27. Siddall, J., Dow Chemical Company, personal communication (2000).
28. Kee, R. J., Dixon-Lewis, G., Warnatz, J., Coltrin, M. E., and Miller, J. A., "A Fortran Computer Code Package for the Evaluation of Gas-Phase Multicomponent Transport Properties," Sandia National Laboratories Report No. SAND86-8246.
29. Kee, R. J., Rupley, F. M., and Miller, J. A., "The CHEMKIN Thermodynamic Data Base," Sandia National Laboratories Report No. SAND87-8215B.
30. Gilbert, R. G., Luther, K., and Troe, J., *Ber. Bunsenges. Phys. Chem.* **87**, 169 (1983).
31. Marinov, N. M., Pitz, W. J., Westbrook, C. K., Castaldi, M. J., and Senkan, S. M., *Combust. Sci. Technol.* **116**, 211 (1996).
32. Stahl, G., and Warnatz, J., *Combust. Flame* **85**, 285 (1991).
33. Lutz, A. E., Kee, R. J., and Miller, J. A., "A Program for Predicting Homogeneous Gas-Phase Chemical Kinetics in a Closed System with Sensitivity Analysis," Sandia National Laboratories Report No. SAND87-8248.
34. Egolfopoulos, F. N., Zhu, D. L., and Law, C. K., *in* "23rd Symposium (International) on Combustion." p. 471, The Combustion Institute, Pittsburgh, PA, 1990.
35. Kee, R. J., Grcar, J. F., Smooke, M. D., and Miller, J. A., "A FORTRAN Program for Modeling Steady Laminar One-Dimensional Flames," Sandia National Laboratories Report No. SAND85-8240.
36. Dagaut, P., Cathonnet, M., and Boettner, J. C., *Int. J. Chem. Kin.* **23**, 437 (1991).
37. Allendorf, M. D., and Zerkle, D. K., in preparation.
38. Rinnemo, M., Deutschmann, O., Behrendt, F., and Kasemo, B., *Combust. Flame* **111**, 312 (1997).
39. Warnatz, J., Allendorf, M. D., Kee, R. J., and Coltrin, M., *Combust. Flame* **96**, 393 (1994).
40. Fisher, G. B., and Gland, J. L., *Surf. Sci.* **94**, 446 (1980).
41. Anton, A. B., and Cadogan, D. C., *Surf. Sci.* **239**, L548 (1990).
42. Wolf, M., Deutschmann, O., Behrendt, F., and Warnatz, J., *Catal. Lett.* **61**, 15 (1999).
43. Wang, P.-K., and Slichter, C. P., *J. Phys. Chem.* **89**, 3606 (1985).
44. Carter, E. A., and Koel, B. E., *Surf. Sci.* **226**, 339 (1990).
45. De La Cruz, C., and Sheppard, N., *J. Catal.* **127**, 445 (1991).
46. Loaiza, A., Xu, M., and Zaera, F., *J. Catal.* **159**, 127 (1996).
47. Duca, D., Botár, L., and Vidóczy, T., *J. Catal.* **162**, 260 (1996).
48. Yeo, Y. Y., Stuck, A., Wartnaby, C. E., and King, D. A., *Chem. Phys. Lett.* **259**, 28 (1996).
49. Zaera, F., Janssens, T. V. W., and Öfner, H., *Surf. Sci.* **368**, 371 (1996).
50. De La Cruz, C., and Sheppard, N., *Phys. Chem. Chem. Phys.* **1**, 329 (1999).

51. Newell, H. E., McCoustra, M. R. S., Chesters, M. A., and De La Cruz, C., *J. Chem. Soc. Faraday Trans.* **94**, 3695 (1998).
52. Cortright, R. D., Watwe, R. M., Spiewak, B. E., and Dumesic, J. A., *Catal. Today* **53**, 395 (1999).
53. Chen, Z., Gracias, D. H., and Somorjai, G. A., *Appl. Phys. B* **68**, 549 (1999).
54. Somorjai, G. A., and Rupprechter, G., *J. Phys. Chem. B* **103**, 1023 (1999).
55. Salmeron, M., and Somorjai, G., *J. Phys. Chem.* **86**, 341 (1982).
56. Berlowitz, P., Megiris, C., Butt, J. B., and Kung, H. H., *Langmuir* **1**, 206 (1985).
57. Godbey, D., Zaera, F., Yeates, R., and Somorjai, G., *Surf. Sci.* **167**, 150 (1986).
58. Windham, R. G., Bartram, M. E., Koel, B. E., *J. Phys. Chem.* **92**, 2862 (1988).
59. Kubota, J., Ichihara, S., Kondo, J. N., Domen, K., and Hirose, C., *Surf. Sci.* **357–358**, 634 (1996).
60. Kubota, J., Ohtani, T., Kondo, J. N., Hirose, C., and Domen, K., *Appl. Surf. Sci.* **121–122**, 548 (1997).
61. Spiewak, B. E., Cortright, R. D., and Dumesic, J. A., *J. Catal.* **176**, 405 (1998).
62. Watwe, R. M., Spiewak, B. E., Cortright, R. D., and Dumesic, J. A., *J. Catal.* **180**, 184 (1998).
63. Wolf, D., Barré-Chassonnery, M., Höhenberger, M., van Veen, A., and Baerns, M., *Catal. Today* **40**, 147 (1998).
64. Hei, M. J., Chen, H. B., Yi, J., Lin, Y. J., Lin, Y. Z., Wei, G., and Liao, D. W., *Surf. Sci.* **417**, 82 (1998).
65. Ohtani, T., Kubota, J., Kondo, J. N., Hirose, C., and Domen, K., *J. Phys. Chem. B* **103**, 4562 (1999).
66. Watwe, R. M., Cortright, R. D., Nørskov, J. K., and Dumesic, J. A., *J. Phys. Chem. B* **104**, 2299 (2000).
67. Goetsch, D. A., Witt, P. M., and Schmidt, L. D., *Heterog. Hydroc. Oxid.* **638**, 124 (1996).
68. Dumesic, J. A., Rudd, D. F., Aparicio, L. M., Rekoske, J. E., and Trevino, A. A., "The Microkinetics of Heterogeneous Catalysis." American Chemical Society, Washington, DC, 1993.
69. Shustorovich, E., and Sellers, H., *Surf. Sci. Rep.* **31**, 1 (1998).
70. Bell, A. T., *in* "Metal-Surface Reaction Energetics" (E. Shustorovich, Ed.). p. 213. VCH, New York, 1991.
71. Williams, W. R., Marks, C. M., and Schmidt, L. D., *J. Phys. Chem.* **96**, 5922 (1992).
72. Campbell, C. T., Ertl, G., Kuipers, H., and Segner, J., *J. Chem. Phys.* **73**, 5862 (1980).
73. Campbell, C. T., Ertl, G., Kuipers, H., and Segner, J., *Surf. Sci.* **107**, 207 (1981).
74. Zhdanov, V. P., and Kasemo, B., *Appl. Surf. Sci.* **74**, 147 (1994).
75. Briot, P., Auroux, A., Jones, D., and Primet, M., *Appl. Catal.* **59**, 141 (1990).
76. "CRC Handbook of Chemistry and Physics" (R. C. Weast, Ed.) p. D-96. CRC Press, Boca Raton, FL, 1985.
77. Benson, S. W., *in* "Thermochemical Kinetics, 2nd ed." p. 22. Wiley–Interscience, New York, 1976.
78. Warnatz, J., Mass, U., and Dibble, R. W., "Combustion: Physical and Chemical Fundamentals, Modeling and Simulation, Experiments, Pollutant Formation." Springer-Verlag, Berlin, 1996.